AB INITIO STUDY OF NANOSTRUCTURES FOR ENERGY STORAGE

A Thesis

by

DAHIYANA CRISTANCHO ALBARRACIN

Submitted to the Office of Graduate and Professional Studies of
Texas A&M University
in partial fulfillment of the requirements for the degree of

MASTER OF SCIENCE

Chair of Committee,	Jorge M. Seminario
Committee Members,	Perla Balbuena
	Hong Liang
Head of Department,	Ibrahim Karaman

May 2014

Major Subject: Materials Science and Engineering

ABSTRACT

Nanomaterials are expected to overcome the challenges imposed from bulk materials in the design of electronic devices. With the help of nanotechnology smaller, lighter, and more energy efficient materials can be used in the development of smart nanodevices. The goal of this research is to characterize the chemical, electrical, and mechanical properties of nanostructures for energy conversion and storage. In this dissertation, three materials are studied at nano level using theoretical calculations: carbon nanotubes (CNTs), lithium silicon ($Li_{4n}Si_n$), and polyvinyl alcohol (PVA). The coupling of mechanical and electronic properties of carbon nanotubes are studied, we estimate a modulus of elasticity of 1.3 TPa and find that the mechanism of CNT structure deformation is chirality dependent. Armchair and chiral nanotubes have ductile deformation fracture while zigzag have both ductile and brittle. Furthermore, the HOMO-LUMO gap of CNT increases under plastic deformation. We conclude that mechanical forces affect the electromagnetic absorption properties of CNTs.

Silicon has been proposed as a promising material for anodes in Li ion batteries; a layer called: the solid electrolyte interphase (SEI) is formed on the electrodes during charging process that may restrict the ion mobility. Preliminary electrical characterization shows the external potential effects of SEI on electron transport as a function of SEI thickness. Furthermore, the rotation of the Li_2O molecules in SEI plays a big role in the electron transport in Li-Ion Batteries.

Mechanical and thermal properties of polyvinyl alcohol (PVA) are characterized using in situ X-ray photoelectron spectroscopy (XPS) and theoretical calculations. It is found that the carbon peaks in PVA shifted under mechanical and thermal stretching. At different temperatures, the C-O bond was the most stable carbon group than others. We find that Hartree-Fock/10-31G (d) reproduces the binding energy of core carbon electrons, which is enough to characterize bonds and corroborate the spectroscopic analysis.

DEDICATION

To my mother: Olga Albarracin, father: Daniel Cristancho, brothers: Daniel and Gerson, and aunt: Jackeline Pulido for their support over the past years.

ACKNOWLEDGEMENTS

I would like to thank my committee chair, Dr. Seminario, and my committee members, Dr. Balbuena, and Dr. Liang for their guidance and support throughout the course of this research.

Thanks also go to the members of the Molecular Electronics group for their help in the group. Furthermore, I want to thank to the agencies supporting this research, the U.S. Defense Threat Reduction Agency (DTRA) through the U.S. Army Research Office, the Assistant Secretary for Energy Efficiency and Renewable Energy, and the Texas A&M Supercomputer Facility. I also want to extend my gratitude to Dr. Holste from Chemical Engineering Department for the opportunity to be a TA in this department.

I want to thank Alba Pineda, Leonardo Gomez, Julibeth Martinez, Jenny Quizena, Paola Leon-Plata, and Diego Ortiz-Vega for their friendship, help, and support during my time at College Station. Thank to my acquaintances, colleagues, the department faculty, and staff for making my time at Texas A&M University a wonderful experience.

Finally, thanks to my mother, father, brothers, and aunt for their encouragement. Thank you, God, for being there for me.

NOMENCLATURE

SEI	Solid Electrolyte Interphase
HOMO	Highest Occupied Molecular Orbital
LUMO	Lowest Unoccupied Molecular Orbital
HLG	HOMO-LUMO gap
CNT	Carbon Nanotube
ITO	Indium tin oxide
UV	Ultraviolet
EC	Ethylene Carbonate
DFT	Density Functional Theory
AB INITIO	First principles
HF	Hartree Fock
B3PW91	Becke Three Perdew Wang Ninety One
LANL2DZ	Los Alamos National Laboratory Doble Zeta
MEP	Molecular Electrostatic Potential
DOS	Density of States
XPS	X-ray Photoelectron Microscopy
MPs	Mechanical Properties
PVA	Polyvinyl Alcohol
BE	Binding Energy

TABLE OF CONTENTS

Page

LIST OF FIGURES

LIST OF TABLES

CHAPTER I

INTRODUCTION

1.1 Advantages of Using Nanostructures in Energy Storage

Due to technological advancement and environmental concerns like global warming due to the burning of fossil fuels, there is a need to design conversion energy and storage energy devices that will be environmentally friendly. The development of this technology depends significantly of the properties of the materials employed to design electronic devices. Currently, nanomaterials are investigated by several research groups to implement them in conversion and energy storage devices because nanomaterials may enhance the performance of these devices due the size confinement. There are several advantages when the size of materials are reduced to nanoscale; for example, nanomaterials improve the stability of electrodes in Li-Ion batteries because they reduce the internal stresses that are produced during charging, reduce the diffusion pathway for lithium ions, and improve the electrode-electrolyte interface area which leads to a higher charge and discharge rates.[1]

Nanostructures are also investigated to be implemented in solar cells devices because these materials improve the energy absorption of these devices by increasing the surface area; also, the manufacturing cost is cheaper. Furthermore, the electronic properties of nanostructured solar cells can be controlled with the size of the material and

nanostructures with different electronic properties can be self-assembled in order to create a multi-junction that adsorbs solar energy in a wider range of the visible spectrum.

1.2 Solar Cells

Solar cells are devices that adsorb sunlight and convert it in electrical current. The solar cells are composed of donor and acceptor materials that are sandwiched between electrodes. The sunlight go through the anode and is absorbed on the donor material that generates excitons (electron-hole pair), which diffuse to the interface of the donor and acceptor. These excitons are separated into positive and negative chargers which are collected in the anode and cathode, respectively. Electrons jump to the LUMO of the donor and then acceptor and holes are created on the HOMO of the donor as shown in Figure 1. The donor is usually made of semiconductor materials with energy band gaps that correspond to the wavelength of the sunlight as is displayed in Figure 2. Research has been conducted in the past years to find semiconductor materials that can be used in solar cells. Carbon nanotubes (CNT), semiconductor materials, have the potential to be implemented in solar cells. First, CNTs are materials made up of carbon which is the fourth most abundant element in the universe; thus, carbon solar cells will be cheap devices at large scales. Second, carbon nanotubes have shown exceptional mechanical[2 3 4] and electronic properties[5 6 7] to be implemented in electronic devices. Third, carbon nanotubes are one of strongest material known so far with modulus of elasticity of ~1TPa; therefore, they do not degrade under the exposure of sunlight and are chemically stable at high temperatures.[8] Lastly, the electronic properties of nanotubes can be tunable with the

size, chirality, diameter, length, and the number of concentric tubes; this feature makes nanotubes a suitable material for the design of any electronic device.

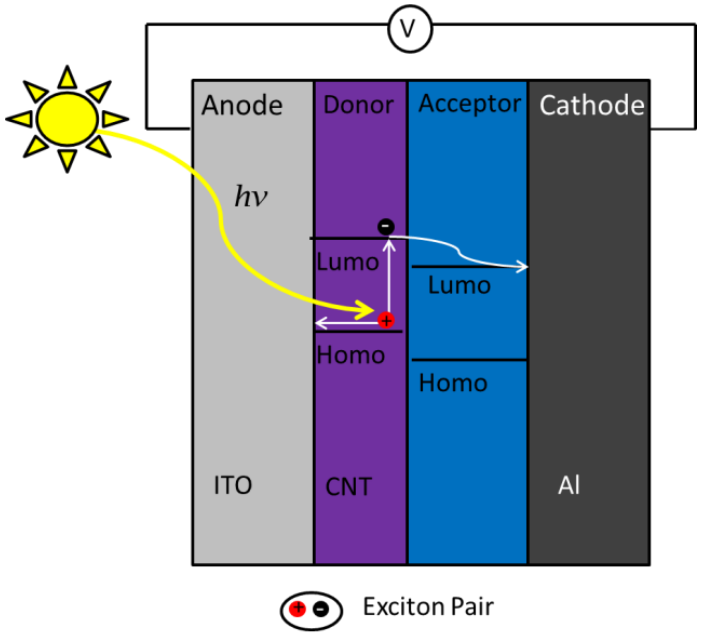

Figure 1. Solar cell heterojunction anode, donor, acceptor, and cathode with the frontier energy levels of the donor and acceptor. Exciton is a pair of electron and hole produced by the absorption of sunlight.

Arnold et al.[9] shown that semiconducting carbon nanotubes surrounded by polymers can be used as donors in solar cells and excitons are capable to dissociate in the interphase of nanotube and fullerene materials. Bindl et al.[10] found that exciton dissociation in the carbon nanotubes/fullerene solar cells is dependent in the diameter of CNTs and the length scale of the nanotube film. Ong et al.[11] reported that pure carbon nanotubes can absorb sunlight and can also form heterojunctions with n-type silicon with a higher conversion

efficiency (2%) than CNTs-polymer solar cells. Ramuz el at.[8] reported the first carbon based solar cell which was fabricated only with carbon materials. These studies demonstrate the potential of carbon nanotubes for the fabrication of solar cells and these materials can effectively be used as donor materials. However, the sunlight absorption, exciton dissociation, and charge collection need to be optimized in order to improve the efficiency of a solar cell.

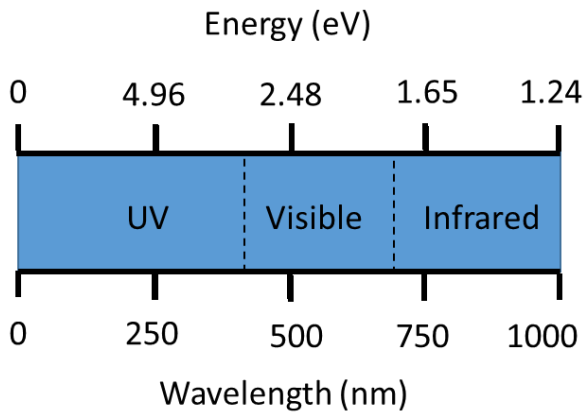

Figure 2. Solar energy spectrum showing the values of the energy and wavelength for the UV, visible and infrared regions.

In this research, the mechanical and electronic properties of carbon nanotubes are investigated with the aim to understand how the mechanical forces affect the electronic properties of carbon nanotubes and to know whether the electronic properties can be tunable by the action of external forces to absorb sunlight in a broader spectrum.

1.3 Lithium Ion Batteries

Li-Ion batteries are commonly used in portable devices like laptops, cellphones, tablets, and also cars. A battery is the organization of various electrochemical cells that are arranged either in series or in parallel with the aim to generate electrical current. The electrochemical cell is consisted of an electrolyte sandwiched between two electrodes (anode and cathode), the electrolyte is a solution that promotes ion conduction between one electrode to the other (Figure 3) and is composed of organic compounds such as ethylene carbonate (EC) and fluoroethylene carbonate (FEC).[12] Lithium ions travel through the electrolyte from the cathode to the anode in charging, and in the opposite direction during discharging, this process is called cycling. The anode enlarges as the lithium ions are adsorbed during charging[13] and the electrolyte degrades electrochemically and generates a layer on the anode surface called SEI that stands for solid electrolyte interphase[14] in the first cycle.

SEI is composed of compounds like lithium fluoride (LiF), lithium oxide (Li_2O), lithium carbonate (Li_2CO_3), and polyethylene oxides $[CH_2CH_2O]_n$.[15] SEI is formed by irreversible reactions that use lithium ions as reactants. SEI film decreases the capacity of the battery[16] and restricts the passage of ions between electrolyte and electrodes. Thus, it is expected that the composition, thickness, stability, and morphology of SEI affect the battery performance as well.[17]

In this research, the composition and thickness of SEI is study to understand how this film affects the electron transport in Li-Ion batteries using molecular simulations and Green function formalism. Also, lithium silicon nanoelectrodes are employed and the size dependence in the electron transport is analyzed.

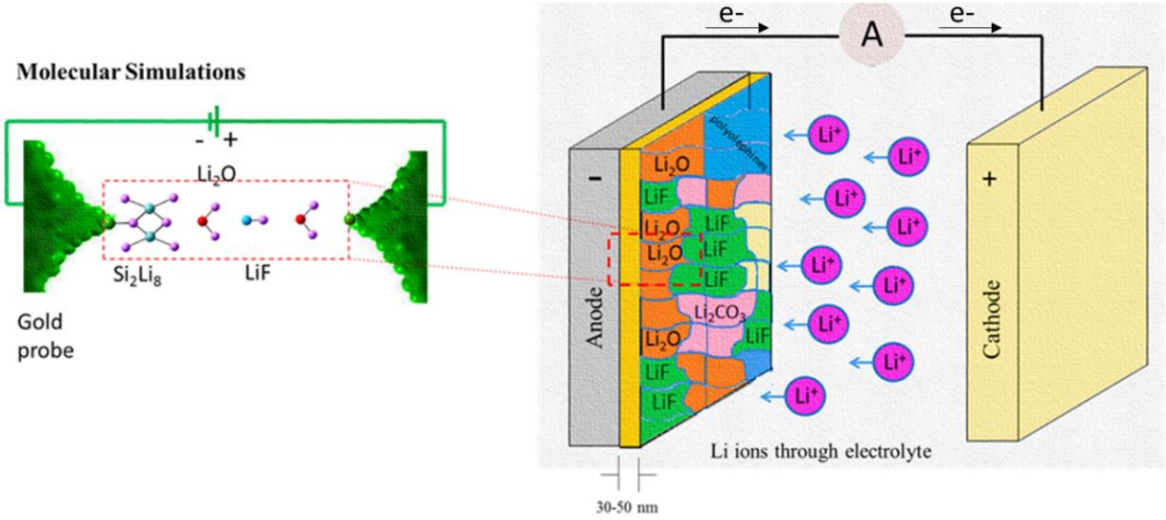

Figure 3. Sketch of the Li-Ion batteries (right) and a piece of the battery (left) proposed to be characterized using molecular simulations.

1.4 Molecular Electronics

Molecular electronics study molecules and clusters of atoms with semiconductor characteristics to be implemented in electronic devices at nanoscale. This is because the final goal of electronic devices is their miniaturization using the smallest system of atoms: molecules. This molecular electronics can be studied using computational tools that involve the use of quantum mechanical methods. Molecular electronics are characterized

by calculating the electrical and electronic properties of the molecules and determine if these molecules can be applied in electronic devices like chemical sensors, energy storage devices, and electronics. Electrical properties are usually determined by calculating the current-voltage characteristics of the molecules or cluster of atoms which are attached to bulk metal contacts that serve as electrodes or probes.

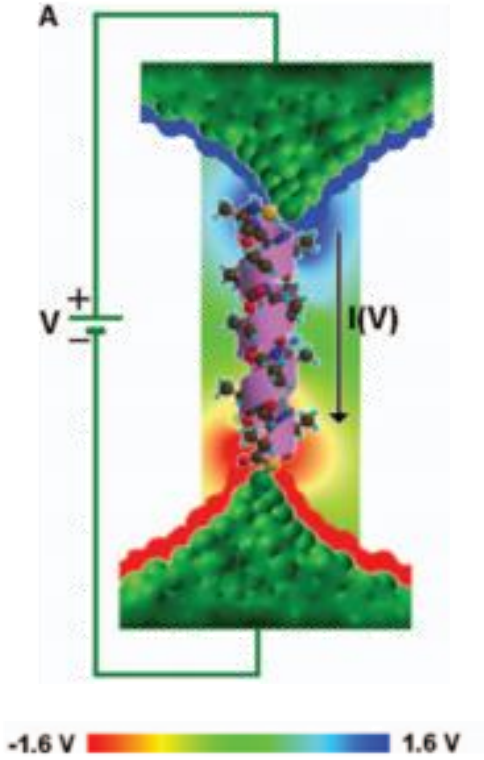

Figure 4. Molecular junction of poly-α-alanine attached to gold contacts (green). The electrical current is measured applying electric field through the molecule using quantum mechanical calculation. Blue and red regions are the positive and negatives potential.[18]

One of the biggest challenges of molecule electronics is the absence of experimental techniques able to reproduce electrical measurement on single molecules connected to bulk electrodes. This is because the lithographic techniques employed nowadays are unable to generate gaps in the order of Angstroms to suspend a single molecule and measure its electrical properties with reproducibility. To overcome this problem, molecular simulations with the help of quantum mechanical methods are employed to study isolated molecules and determine its current-voltage characteristics with precision and reproducibility. DFT methods and Green Function are combined to calculate the current-voltage curves. These methods are described below in chapter II. Figure 4 shows a single molecule (poly-alanine) attached to bulk gold, Cristancho et al.[18] found that this single molecule has a diode behavior which is the behavior of an electronic element with asymmetric current-voltage characteristics and this is an example of how single molecules are well studied using DFT-Green function procedure.

CHAPTER II

MOLECULAR MODELING AND THEORY

2.1 Ab Initio Molecular Orbital Theory

Total energy and properties of materials can be calculated by solving the Schrodinger equation:

$$\mathrm{H}\,(\mathrm{r},\mathrm{R})\psi(\mathrm{r},\mathrm{R}) = \mathrm{E}(\mathrm{R})\,\psi(\mathrm{r},\mathrm{R}) \qquad (1)$$

$E(R)$ is the energy of the molecular system, $\psi(r,R)$ is the wave-function, and $H(r,R)$ is the Hamiltonian. The wavefunction represents the probability of finding electrons of the system at given time and space (r). And the Hamiltonian is an operator that denotes the total energy of the system that is composed of the kinetic (E_k) energy plus and potential (V) energy as it is described as follows:

$$\mathrm{H} = \mathrm{E_k} + \mathrm{V} = -\frac{\hbar^2}{2\mathrm{m}}\nabla^2 + \mathrm{V}(\mathrm{r},\mathrm{t}) \quad \nabla^2 = \frac{\partial^2}{\partial^2\mathrm{x}} + \frac{\partial^2}{\partial^2\mathrm{y}} + \frac{\partial^2}{\partial^2\mathrm{z}} \qquad (2)$$

Where ħ is the reduce Planck constant, m is the mass, and ∇ is the Laplace operator. The Schrodinger equation can be solved using AB INITIO and semi-empiric methods. These methods are based on either density functional theory (DFT) or Hartree-Fock (HF) as is explained below.

2.1.1 Density Functional Theory (DFT)

DFT was introduced by Hohenberg-Kohn[19] and Kohn-Sham[20] and is a quantum mechanic method that uses functionals, function that uses a function as input and provides a number as an output, of the electron density to determine the properties of a molecular system without using the wave function. The electron density depends of the spatial coordinates x, y, and z. All the properties of a ground state system can be determined using DFT. The Hamiltonian is determined by the kinetic energy, the external potential, and the electron-electron interaction: [21]

$$\widehat{H} = -\frac{1}{2}\sum_{i}^{N} \nabla^2{}_i + \widehat{V}_{ext} + \sum_{i<j}^{N} \frac{1}{|r_i - r_j|} \quad (3)$$

$$\widehat{V}_{ext} = -\sum_{\propto}^{N_{at}} \frac{Z_{\propto}}{|r_i - R_{\propto}|} \quad (4)$$

Where r_i is the electron coordinate, R_α and Z_α are the coordinate and charge of the nucleus, respectively.

2.1.2 Hartree- Fock (HF)

Hartree-Fock is a quantum mechanic method that determines the wave function of a molecular system by using the Slater determinant:

$$\psi_{HF} = \frac{1}{\sqrt{N!}} \begin{vmatrix} \psi_1(\overrightarrow{x_1}) & \dots & \psi_N(\overrightarrow{x_1}) \\ \psi_1(\overrightarrow{x_2}) & \dots & \psi_1(\overrightarrow{x_2}) \\ \psi_1(\overrightarrow{x_N}) & \dots & \psi_N(\overrightarrow{x_N}) \end{vmatrix} \quad (5)$$

Where ψ_{HF} is the wavefunction, N is the spin orbitals, and ψ_i are orthogonal orbitals. The local minimum of molecular system is determined by finding the orthogonal orbitals that minimize the total energy of the wave function.

$$E_{HF} = \int \phi_i^*(r)\left(-\frac{1}{2}\sum_i^N \nabla_i^2 + V_{ext}\right)\phi_i(r)dr +$$

$$\frac{1}{2}\sum_{i,j}^N \int \frac{\phi_i^*(r_1)\phi_i(r_1)\phi_j^*(r_2)\phi_j(r_1)}{|r_i - r_j|} dr_1 dr_2 - \frac{1}{2}\sum_{i,j}^N \int \frac{\phi_i^*(r_1)\phi_j(r_1)\phi_i(r_2)\phi_j^*(r_2)}{|r_i - r_j|} dr_1 dr_2 \quad (6)$$

Where the second and third terms correspond to Columbic interaction and exchange energy, respectively. $\phi_i(r)$ is the wavefunction.

2.2 Hybrid Functional

Hybrid functional is a combination of Hartree-Fock and Ab Initio. Examples of these are the B3PW91 that stands for Becke Three[22] (3 parameters) which uses the Perdew and Wang (PW91)[23] 1991 correlation functional. This functional is used mostly in all the performed calculations of this research.

2.3 Basis Sets

Basis sets (f_μ) are linear combinations of Gaussian primitives (g_l) functions with the form:

$$f_\mu = \sum_{l=1}^{L_\mu} d_{l\mu} g_l(x, y, z) \quad (7)$$

$$g_l(x, y, z) = N_l x^a y^b z^c e^{-\alpha_l r^2} \quad (8)$$

Where L_μ is the number of Gaussian primitives, $d_{l\mu}$ is a coefficient, a, b, c are integers and N_l and α_l are constants. The nomenclature of a basis set is N-M1G (double zeta basis set) or N-M11G (triple zeta basis sets) where N and M are integers. In this research basis sets like 6-31G* and 3-21G are used in the calculations, where the first number indicates the Gaussian primitives of the core orbital function, the two numbers after the dash represents that the basis sets are split valence double zeta and represent the valence orbitals, G means that Gaussian primitives are used in the basis function, and the * indicates that d polarization functions are added for all atoms, except hydrogen. Also, LANL2DZ[24 25] basis set is also used in this research for the valence orbital of the metals where LANL is los Alamos National Laboratory and DZ is the double zeta.

2.4 Molecular Electrostatic Potential (MEP)

Molecular electrostatic potential is a potential that a molecule builds due to the nucleus and electrons. This electrostatic potential is associated with the electron density through:[26]

$$V(r) = \sum_A \frac{Z_A}{|R_A - r|} - \int \frac{\rho(r')dr'}{|r' - r|} \quad (9)$$

Where V(r) is the potential, Z_A is the charge on the nucleus, r is position coordinate, and $\rho(r')$ is the electron density. MEP is useful because it gives information about the distribution of nuclear and electronic charges on a molecule and is commonly used to determine chemical reactivity in a molecular system. MEPs are good indicative of negative potentials which are also used to determine cation mobility pathway of Li-Ion batteries. The MEPs are calculated using the program Gaussian 09[27] from the output files of calculation of structure optimization.

2.5 Molecular Orbital (MO)

Molecular orbitals are functions that represent the behavior of an electron in a molecule. Molecular orbitals are formed of atomic orbitals that are also functions used to describe the behavior of an electron but in an atom. Molecular orbital spectrum is the representation of lines that correspond to the energy of every molecular orbital. Degeneracy of molecular orbitals is represented by several lines at the same energy. According to Pauli Exclusion Principle, two electrons with opposite spin (spin up and down) occupy one level of energy (one line). In the MO spectrum is divided in two sections: occupied and unoccupied molecular orbitals where the highest occupied molecular orbitals is the HOMO and the lowest unoccupied molecular orbital is the LUMO. These are called the frontiers orbitals and the difference between HOMO and LUMO is the HOMO-LUMO gap. The HOMO-LUMO gap is important in predicting whether a material behaves as metallic, semiconductor, or insulators as shown in Figure 5. According to the theory of bands, the occupied orbitals that are close to the HOMO corresponds to the valence band and the

unoccupied orbitals are the conduction band. In the conduction band the electron move freely. In metal, the conduction and valence band overlap, semiconductors has a small band gap and insulator has large band gaps.

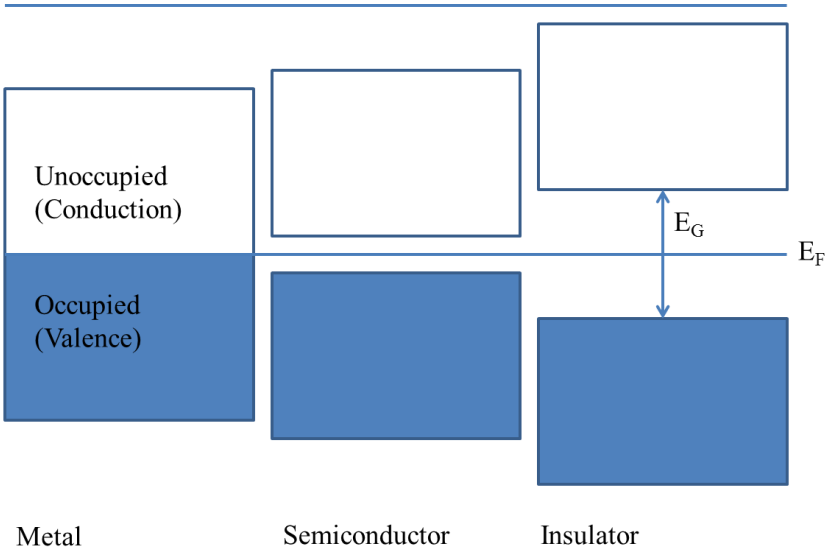

Figure 5. Energy diagram of metal, semiconductor, and insulator materials. Where Eg is the band gap energy (HOMO-LUMO gap) and EF is the Fermi energy.

Understanding the MO diagram or band structures of materials is important in the design of electronic devices. In this research the molecular orbitals diagram will be employed to study nanostructures like carbon nanotubes for solar cells and lithium-silicon electrodes in Li-Ion batteries. Materials that are suitable candidates to be part in solar cells must have a HOMO-LUMO gap that corresponds to the wavelength of the sunlight.

2.6 Density of States (DOS)

The density of states is a mathematical function that relates the number of states per energy available to be occupied for electrons.

$$N = \int_{E_1}^{E_2} \rho_{energy}(E)dE \tag{10}$$

Where N is the total number of states from E_1 to E_2 and ρ_{energy} is the density of states/energy which can be calculated in 3D using:

$$\rho_{energy} = \frac{g(E)}{volume} \tag{11}$$

$$g(E) \sim \frac{dn}{dE} \tag{12}$$

g(E) is the energy density and n is the number of levels.

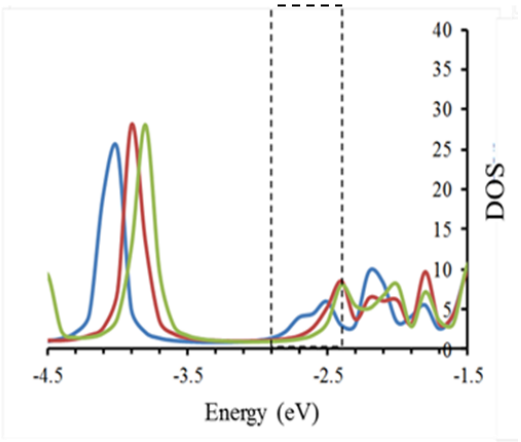

Figure 6. Example of a density of states spectrum (g(E)).

Figure 6 shows an example of a DOS spectrum where y-axis is the energy density and x-axis is the energy. High DOS at a value of energy indicates the amount of states to be occupied and no DOS means that there are not states available to be occupied. DOS will be used in this research to calculate the current-voltage characteristics of materials by mixing the DOS of gold atoms (electrodes) with the Hamiltonian of the molecular system.[18] Computational tools like CRYSTAL[28] and GaussSum[29] are used to extract the DOS of the molecular simulations.

2.7 Current-Voltage Characteristics (I-V)

Current-voltage characteristics are used in this research to characterize Li-Ion Batteries using the generalize electron nanointerface program (GENIP). The I-V are calculated using the transmission function *T(E,V)* using the Launder equation:[25]

$$I \approx \frac{2e}{h}\int_{E_f+V_1}^{E_f+V_2} T(E,V)dE \qquad (13)$$

Where e is the charge of the electron, h is the Planck constant, *T(E,V)* is the transmission function, *E* is the energy, V the voltage, and E_f is the Fermi level of the molecular junction.

The transmission function is calculated using the following expression: [30] [31] [32]

$$\mathrm{T(E,V)} = \mathrm{Trace}(\mathrm{T_1(E,V)G_M(E,V)T_2(E,V)G_M^{+}(E,V)} \qquad (14)$$

$T_k = i(\sum_k - \sum_k^+)$ with k=1,2 (2 electrodes) is the coupling between the electrodes and the molecule, [22] [21] G_M is the retarded Green function and G_M^+ is its adjoint. G_M is obtained using:

$$G_M(E,V) = [ES_{MM}(E,V) - H_{MM}(E,V) - \sum_1(E,V) - \sum_2(E,V)]^{-1} \quad (15)$$

$$\sum_i(E) = (ES_{Mi} - H_{Mi})(ES_{iM} - H_{iM}) \quad (16)$$

Where i=1,2. S_{iM} is the overlap submatrix and H_{iM} is the Hamiltonian of the molecule which are obtained from the Schrondinger equation. $\sum_i(E)$ is the self-energy that helps to the broadening of the molecular levels and it is dependent of the Green's function g_i:

$$g_i = \pi i \begin{pmatrix} g_{i1} & \dots & 0 \\ \vdots & \ddots & \vdots \\ 0 & \dots & g_{iN} \end{pmatrix} \quad (17)$$

g_{iK} elements are calculated using:

$$g_{iK} = \begin{bmatrix} (D_s)_{iK}(E) & 0 & 0 & 0 \\ 0 & (D_p)_{iK}(E) & 0 & 0 \\ 0 & 0 & (D_{t2g})_{iK}(E) & 0 \\ 0 & 0 & 0 & (Dd_{eg})_{iK}(E) \end{bmatrix} \quad (18)$$

2.8 X-ray Photoelectron Microscopy (XPS)

XPS is a spectroscopy technique to characterize surface chemistry of a material specifically to determine elemental composition. This technique uses X-rays to eject core electrons, these electron do not participate in the bonding of atoms, from the material's surface. Although this technique is for core electrons, chemical shift occurs due to the type of bonding of the atom. Einstein equation gives the relationship between binding energy of the core electrons and the energy of the X-rays by:

$$E_B = hv - E_k \quad (19)$$

Where E_B is the binding energy, *hv* is the X-ray energy, and E_k is the kinetic energy of the core electron. E_B is obtained from the difference of the final and initial energy of the atom with and without core electrons.

$$E_B = E_{final}(n-1) - E_{initial}(n) \quad (20)$$

Where n is the number of electrons. The final state corresponds to the energy of the atom without one electron (ion). The final energy is lower than the initial because in the final states the electrons relax. The binding energy of the core electrons at vacuum is proportional to the orbital energy according to the Koopmans' theorem:

$$E_B = -\varepsilon_n \quad (21)$$

In this research, XPS measurements of polyvinyl alcohol (PVA) samples are corroborated using molecular orbital theory by analyzing the molecular orbital energy of the core electrons of carbon and oxygen atoms in PVA mers. Relativistic, relaxation, and electron correlation effects have to be considered for the calculation of the binding energy using the orbital energy:

$$E_B(k) = -\varepsilon_n - \delta\varepsilon_{relax} + \delta\varepsilon_{rela} + \delta\varepsilon_{corr} \quad (22)$$

CHAPTER III

COUPLING OF MECHANICAL AND ELECTRONIC PROPERTIES OF CARBON NANOTUBES *

3.1 Carbon Nanotubes

Carbon nanotubes are tubes made of carbon atoms with size at the nanoscale. Every carbon atom is attached to three neighboring carbon atoms which are bonded through covalent bonds (sharing of electrons), which form a periodic network of hexagonal rings with a tube-like conformation. Carbon atoms are classified in the fourth column of the periodic table with an atomic number of six that leads to an electronic configuration of $1s^2 2s^2 2p^2$ with two core electrons and four valence electrons which occupy 2s and 2p orbitals. When carbon atoms bond to form carbon nanotubes, the valence orbitals mix and create three sp^2 hybrids with one unhybridized p orbital. The lobes of p orbitals overlap and form π-bonds in carbon nanotubes. These π bonds generate a delocalized electron cloud along the nanotube.

Carbon nanotubes are illustrated as the rolling up of one graphene sheet and depending on the number of graphene that are rolled up concentrically to form nanotubes, CNTs can be either single-wall carbon nanotubes (SWCNT) or multi-wall carbon nanotubes (MWCNT).

---

* This chapter is reprinted with permission from:
Coupling of Mechanical and Electronic Properties of Carbon Nanotubes, by D. Cristancho, L. Benitez, and J.M. Seminario, 2013. J. Mol. Model. 19. 5237-5244.

SWCNT is made of one single sheet of graphene that is rolling up tubularly. MWCNT are concentric SWCNTs that are separated radially with a distance of approximately 0.36 nm. SWCNTs are held together by Van der Waals forces. SWCNTs and MWCNTs lengths are up to 1μm with a diameter range from 1 nm to 50 nm. In this research the mechanical and electronic properties of SWCNT will be studied. From now on, SWCNT will be abbreviated as CNT. CNTs are classified according in the angle direction that graphene sheet is rolling up into a nanotube. This rolling up is characterized by both the chiral vector (C_h) and chiral angle (θ), which control the chirality or helicity (angle of growth), diameter, and length of CNTs. C_h is the sum of the lattice vectors a_1 and a_2, and is defined as follows:

$$C_h = na_1 + ma_2 \equiv (n, m) \tag{23}$$

Where *n* and *m* are integers ($0 \leq m \leq n$). C_h is perpendicular to the tube axis and the chiral angle θ is the angle between C_h and a_1 which is defined in terms of (*n*,*m*) as:

$$\cos(\theta) = \frac{2n+m}{2\sqrt{n^2+m^2+nm}} \tag{24}$$

With a range: $0 \leq \theta \leq 30°$.

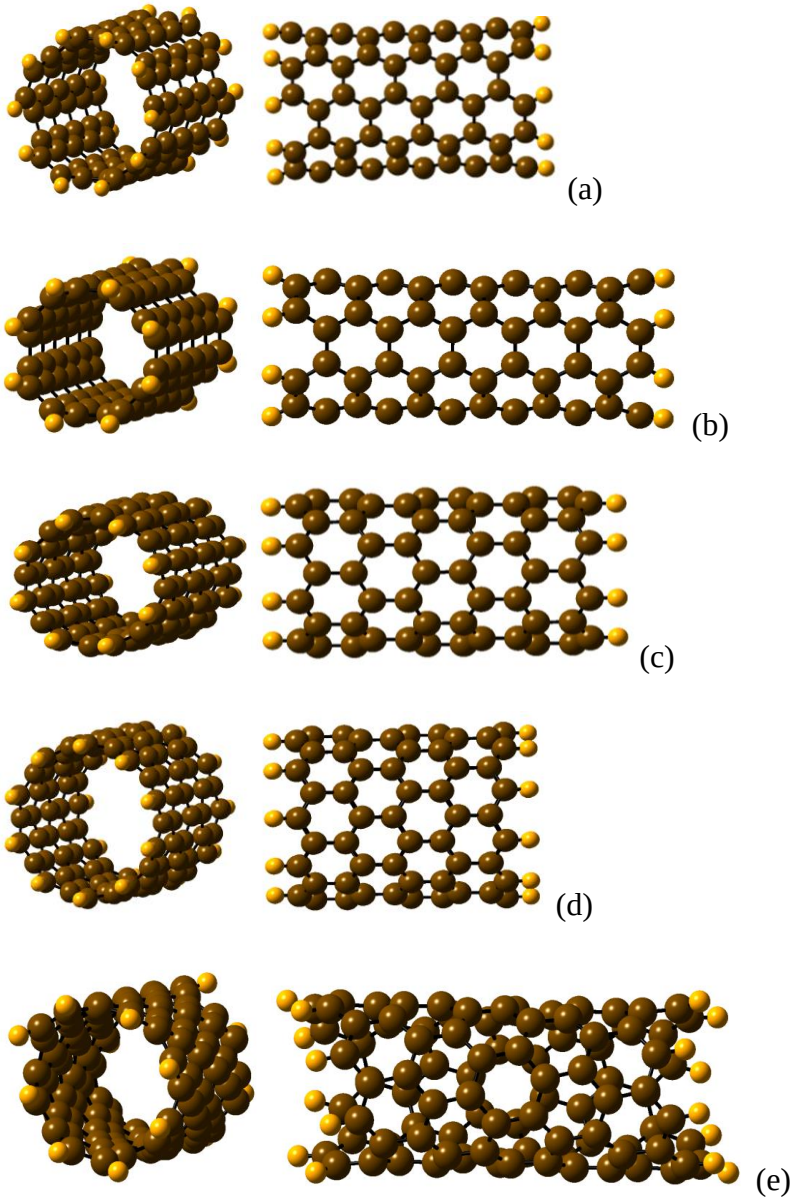

Figure 7. Longitudinal (left) and side (right) views of optimized carbon nanotube structures used in the current study. (a) CNT(5,5) (b) CNT(4,4) (c) CNT(8,0) (d) CNT(10,0) and CNT(6,2). C: brown, H: yellow.

Table 1 shows the classification of CNTs with their corresponding chiral angle (θ) and chiral indices (*n*,*m*).

The diameter of carbon nanotubes can be also determined theoretically using the integers *n* and *m* as follows:

$$d = \frac{a}{\pi}\sqrt{(n^2 + nm + m^2)} \quad (25)$$

Where *a* is the lattice constant (*a*=2.49 Å). Experimentally, CNTs' diameter and lengths depend significantly on the synthesis conditions such as temperature, catalyst, and time.[33] Therefore, there are three types of CNTs: zigzag, armchair and chiral as displayed in Figure 7.

Table 1. Classification of CNTs according how graphene sheet is rolling up with their corresponding chiral angles (θ) and chiral indices (n,m).[34]

CNT	(n,m)	(θ)
Zig-zag	(*n*,0)	0
Armchair	(*n*,*n*)	30°
Chiral	(*n*,*m*) $n \neq m \neq 0$	$0 < \theta < 30°$

In this research armchair CNT (4,4), CNT (5,5), zigzag CNT (8,0), CNT (10,0), and chiral CNT (6,2) nanotubes are used to study the coupling of mechanical and electronic properties of CNTs.

3.2 Literature Review

Despite of the technological advancement that has been done in the past years, experimental characterization of the mechanical properties (MPs) of advanced materials at the nanoscale is still challenging because the small size of the structures makes manipulation, observation, and measurement of applied forces not very accurate.[35] Hence, quantum mechanical calculations offer the advantage of determining very precisely, the physical-chemical properties of molecular systems and give a good estimation of the molecular structure, orbitals, and defects of a material under external forces; most of these properties are difficult to observe experimentally. Molecular modeling is also important to get initial or guess parameters for the design of new nanomaterials and nanodevices. A new nanomaterial in a mechanical assembly is subject to external forces that stretch, deform and, if the applied loads are in excess, destroy the material. Thus, it is important to know whether the material will be strong enough to resist the loads that it will suffer during service. For this reason, scientists have focused in the search and design of tensile tests using several methodologies and approaches to characterize the MPs of nanostructures such as carbon nanotubes (CNT).

Properties such as the modulus of elasticity (*E)* of CNT have been reported using experimental techniques and theoretical approaches (Table 2). Experimentally, MPs of CNTs have been studied primarily using two microscopy techniques: the transmission electron microscopy (TEM),[36] and the atomic force microscopy (AFM).[2] Treacy et al.[37] found, for the first time, a value of 1.8 TPa for the elastic modulus of CNT using TEM by

observing the thermal vibrations, and *E* was estimated from the frequencies of the first two resonant modes.[38] In 2007, Wong et al.[36] found a value of 1.28 TPa by using AFM to bend multiwall carbon nanotubes (MWCNTs), and then measuring their deflection as a function of the applied force and as a function of the displacement from its equilibrium;[36] *E* was extracted from the slope of the deflection versus force curve.[2] Nonetheless, using AFM or TEM might hamper observing the details of the atomic structures, deformations, dislocations, crack propagations, and faults at every point of the stress-strain curve. The identification of these defects allows further explanation of the changes in the CNTs MPs and plays important roles in processes such as deformation, annealing, diffusion,[39] widening in this way the number of CNT applications.

Table 2. Modulus of elasticity (E) using several approaches. Data from Krishnan et al.,[40] Van Lier et al.,[41] Li and Chou,[4] Natsuki et al.,[42] Pantano et al.,[43] Gupta et al.,[44] and Wu et al.[45] is taken from Khoury et al.[46] Finite element methods (FEM).

Year	Authors	Method	*E* (TPa)
1996	Treacy et al.[37]	Transmission electron microscopy	1.8
1997	Wong et al.[36]	Atomic force microscopy	1.28
1998	Krishnan et al.[40]	Thermal vibrations	1.30
2000	Van Lier et al.[41]	Ab initio	1.14
2003	Li and Chou.[4]	Structural Mechanics	1.04
2004	Mylvaganam et al.[47]	Molecular dynamics	4.88
2004	Natsuki et al.[42]	Molecular structural mechanics	1.10

Table 2. Continued.

Year	Authors	Method	*E* (TPa)
2004	Natsuki et al.[42]	Molecular structural mechanics	1.10
2004	Pantano et al.[43]	Continuum shell modeling	4.75
2005	Gupta et al.[44]	Hydrostatic pressure	1.22
2006	Wu et al.[45]	Molecular mechanics	1.06
2008	Wu et al.[48]	STM and magnetic actuation	0.97
2009	Rossie et al.[3]	Molecular Mechanics	0.92
2010	Shokrieh et al[49]	Nanoscale Continuum Mechanics	1.04
2011	Arenal et al.[50]	HRTEM/AFM	1.11
2012	Rafiee and Heidarhaei [51]	Non Linear FEM	1.33

MPs and thermal properties of CNTs are attributed to their unique structure of covalent (shared) bonding of sp^2 hybridized carbon atoms forming strong σ and π bonds between carbon atoms.[5] CNT average elastic modulus of ~1.18 TPa and thermal conductivity[52] of 3,500 $Wm^{-1}K^{-1}$ are comparable to those of diamond, 1.22 TPa and 3,320 $Wm^{-1}K^{-1}$,[53] respectively. Because of these properties, CNTs are commonly used in composites[54] to reinforce materials such as polymers,[55] ceramics, and metals.[56]

Therefore a deep understanding of the relation between mechanical and electronic properties is important to expand the implementation of CNTs in practical applications; for example, in energy storage devices, Ren et al.[57] studied twisted MWCNTs/MnO_2 and

found that this composite can be employed as electrode to create both supercapacitors and lithium-ion microbatteries, and thus introduced carbon nanotubes in the field of conventional energy storage systems. Among CNTs current applications are graphene nanoribons,[58] drug delivery systems,[59] tips for atomic force microscopy (AFM),[60] scaffolds for bone growth,[61] synthetic muscles,[62] composites,[63] coatings,[64] solar cells,[65] lasers,[66] concretes,[67] potent strength fibers,[68] and fire prevention.[69]

Recently, we studied the functionalization of carbon nanotubes with poly(ethylene glycol) for drug delivery applications,[70] the design of self-assembled DNA-CNT,[71] the interactions of DNA and CNTs,[72] and also the mechanism of the unzipping of CNTs using potassium permanganate for the fabrication of graphene nanoribbons.[73] Here, we extend our understanding of CNTs, by calculating and studying the relationship between their mechanical and electronic properties. Although, the measurement of the mechanical properties of carbon nanotubes has been the focus of several research studies, there is still a controversy or doubts on whether carbon nanotubes are the stiffest materials known so far. In this study, we calculate the elastic modulus of CNTs, determine their stress versus strain curve, analyze their deformation structure until fracture, and finally correlate their mechanical properties with electronic properties, using ab initio quantum mechanic calculations.

3.3 Methodology

In this work, CNT (n,n), n = 4, 5; CNT (n,0), n = 8, 10; and CNT (6,2) are analyzed to calculate their modulus of elasticity; they are passivated with hydrogen atoms at their dangling ends to transform the edge carbon atoms into coordination three sites, and to avoid reconstruction of the atomic structure after optimization (Figure 7). First, all the initial geometries are optimized to a local minimum using the unrestricted B3PW91/6-31G(*d)* level of theory[74] as coded in the program Gaussian 09.[27] Local minima are tested by performing second derivative calculations only for optimized geometries under zero strain. As initial guess, the highest occupied molecular orbital (HOMO) and the lowest occupied molecular orbital (LUMO) are mixed to break α and β spatial symmetries. Then, each carbon nanotube is strained and re-optimized by keeping the hydrogen and carbon atoms located at the ends fixed at their strained locations. At every applied strain, the inner atoms adopt their most stable conformation after each optimization. This procedure is repeated until the CNTs fracture.

For a CNT of radius r and length L, the modulus of elasticity ($E = \sigma/\varepsilon$) is calculated as the slope of the linear (elastic) slope of the stress (σ) versus strain ($\varepsilon = \Delta L/L$) curve. The stress σ (F/A) is the applied force divide by cross section area ($A = \pi r^2$) of the CNT and ΔL is the change of length of the CNT when the force (F) is applied along its axis. If the total energy of the CNT is W, then $F = dW/dL$.

In this work, the yield strength (f_y) is calculated using an offset of 0.002, the tensile strength (f_T) is calculated as the maximum of the stress-strain curve, the fracture point (f_F) is computed as the last point in the stress-strain curve (f_F, ε_F), and the toughness (Ω) as:

$$\Omega = \int_0^{\varepsilon_F} \sigma d\varepsilon \quad (26)$$

3.4 Mechanical Properties

Figure 8 shows the stress-strain curve of CNT (n,n), n = 4, 5; CNT (m,0), m = 8, 10; and CNT (6,2). Three behaviors of the materials are observed in the curve: elastic, plastic, and fracture. It is found that the stress is directly proportional to strain in the elastic region with an average elasticity modulus of 1.31 TPa (Figure 8) and this calculated value is in good agreement with those reported in the literature (Table 2). CNT (8,0) is the stiffest and CNT (5,5) is the most flexible with a modulus of elasticity of 1.91 TPa and 0.94 TPa, respectively (Table 3). This difference is because in the zigzag the stretching affects mainly an angular bending but a bond stretching in the armchair; this later bond eventually breaks (Figure 9).

In addition, both ductile and brittle behaviors are observed in the stress-strain curve; CNT(4,4), CNT(5,5), CNT(8,0), and CNT(6,2) behave as ductile materials with plastic deformation whereas CNT(10,0), which is fractured while is deformed elastically, behaves as a brittle material. These behaviors were also observed by Coluci et al.[75] who also studied the mechanical properties of carbon nanotubes and found that zigzag and armchair

nanotubes behave as brittle and ductile materials, respectively. In all of the CNTs structures examined in the current study, except CNT (10,0), the stress increases to a maximum stress (f_T) and then decreases to the final fracture (f_F). CNT (10,0) stress increases and stops at the maximum point f_T of 0.13 TPa which is equal to f_F. However, CNT (4,4), CNT (5,5), CNT (6,2), and CNT (8,0) experience plastic deformation because they have a maximum value of f_T that differs from its fracture value, f_F (Table 3).

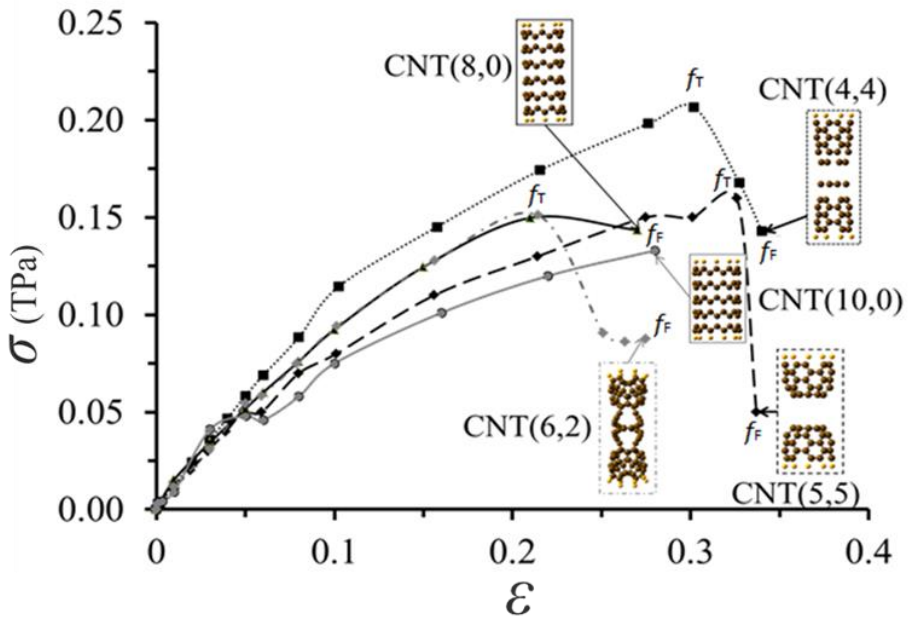

Figure 8. Tensile strength (f_T), fracture (f_F) and stress (σ) versus strain (ε) points for CNT (n,n) with n = 4, 5; CNT (m,0) with m = 8, 10; and CNT (6,2). The calculated E are 1.2, 0.94, 1.91, 1.45 and 1.01 TPa, respectively. All structures are optimized.

Every nanotube structure undergoes different fracture pathways, which are chirality dependent (Figure 8). We re-optimized the geometries of CNTs at every point of the stress-strain curve. We find that armchair nanotubes deform and fracture plastically; once

the external stress goes beyond f_T, the nanotubes experience *necking*, which is confirmed by a decrease in the diameters of CNT(4,4), and CNT(5,5) from 0.553 to 0.407 nm and from 0.881 to 0.462 nm, respectively.

Two structures are found for CNT (5,5) at fracture point. The fracture point structure with the lowest energy forms two well-defined caps that can be thought as half-fullerenes (hollow sphere made of carbon atoms) with 16 hexagons, and 10 squares. However, the structure with the highest energy breaks into four pieces; two of them are rings of carbon dimers and the other two are conformed of carbon hexagon without deformation in the radial direction. These fracture point structures are created by the reorganization of carbon atoms and the formation of new σ and π-bonds due to the high reactivity of the carbons from the broken bonds, which finally reconstruct to a minimum energy conformation. CNT (4,4), which is the most ductile nanotube with a toughness of 4.32 $J/m^3 \times 10,^{10}$ breaks into four pieces: two rings that are conformed by carbon dimers and two caps of only hexagons (Figure 8). Carbon dimers are formed when running the CNT (4,4) as a closed shell singlet, which has energy 1,084.5 kcal/mol lower than the corresponding triplet.

On the other hand, fracture of zigzag CNTs takes place without any significant deformation of the structure in the radial direction (Figure 8); these nanotubes distort only in the direction of the applied stress or axial direction and start cracking in several parts along the axis when they are strained 21% of their length (Figure 8). Chiral fracture occurs in three stages: first, carbon-carbon bonds that are located parallel to the direction of the

applied stress are broken, increasing their length from 0.142 nm to 2.11 nm, ending in a spiral-shaped conformation which can be thought as the wrapping of two carbon chains. Next, as stretching continues, carbon atoms displace in the direction of the applied stress, and finally, fracture results with the formation of two caps with topological defects (ten hexagons, two pentagons, and two triangles) that are separated by the two carbon chains, in helix conformation and sp^3 hybridization (Figure 8).

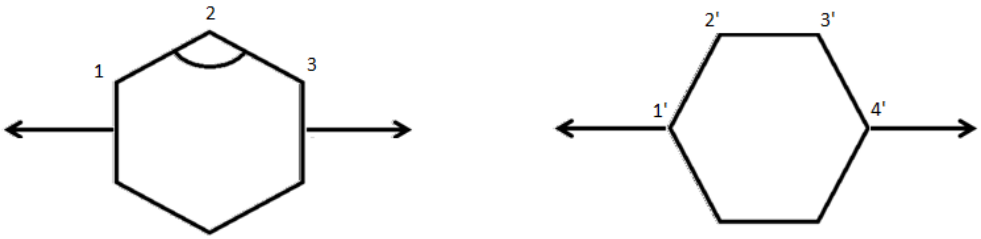

(a) (b)

Figure 9. The direct effect of a longitudinal stress on an (a) armchair and (b) zigzag CNTs correspond to angular bending and bond stretching, respectively.

The mechanical properties obtained from the strain-stress curves (Figure 8) yield higher toughness (3.94×10^{10} J/m^3) for armchair than for zigzag (2.58×10^{10} J/m^3) and chiral (2.48×10^{10} J/m^3) carbon nanotubes (Table 3). This occurs because armchairs have higher capacity to deform plastically and to propagate cracks than chiral and zigzag do. This behavior takes place because armchair nanotubes are deformed in both, axial (along the

applied stress) and radial directions; on the other hand, zigzag is deformed in the axial direction only and chiral deform by untangling carbon chains. Therefore, nanotubes that are deformed in axial and radial directions absorb higher energy which is used for the crack propagation and the microvoid coalescence process (mechanism of fracture in ductile materials).

Table 3. Young modulus (E), yield strength (f_y), tensile strength (f_T), fracture (f_F), and toughness (Ω) of CNTs. All mechanical properties are in TPa except for Ω which is J/m^3.

CNT	C_nH_n	Point Group	E	f_y	f_T	f_F	Ω ($\times 10^{10}$)
(4,4)	$C_{95}H_{16}$	D_{4d}	1.20	0.07	0.19	0.13	4.32
(5,5)	$C_{100}H_{20}$	D_{5d}	0.94	0.04	0.02	0.06	3.56
(8,0)	$C_{96}H_{16}$	C_1	1.91	0.02	0.15	0.14	2.78
(10,0)	$C_{100}H_{20}$	C_{2V}	1.50	0.05	0.13	0.13	2.37
(6,2)	$C_{100}H_{16}$	D_2	1.01	0.06	0.15	0.28	2.48

3.5 Electronic Properties

To understand the mechanical behavior of carbon nanotubes, frontiers orbitals are calculated using molecular orbital theory. Figure 10 displays the molecular orbital spectra of all nanotubes used in the current study with their corresponding frontier orbital shapes at points from the elastic region, f_y, f_T and f_F. CNT (4,4) HOMO lies at -4.25 eV and has a delocalized orbital that is perpendicular to the stretching direction, while CNT (5,5)

HOMO lies at -4.48 eV and has a delocalized orbital along the pulling direction. Delocalization of frontier orbitals is due to the overlapping of the *p* atomic orbitals that do not participate in the σ bonds. As stretching of CNT (4,4) and CNT (5,5) occurs from 0 to 0.04 and from 0 to 0.002, respectively, their HOMO-LUMO gap increases from 1.26 eV to 1.61 eV and decreases from 1.70 eV to 1.67 eV, respectively. Their molecular orbitals keep delocalized on the CNT surface as a consequence of the stability of armchair CNTs under elastic stretching, and the flexibility of the carbon-carbon bonds.

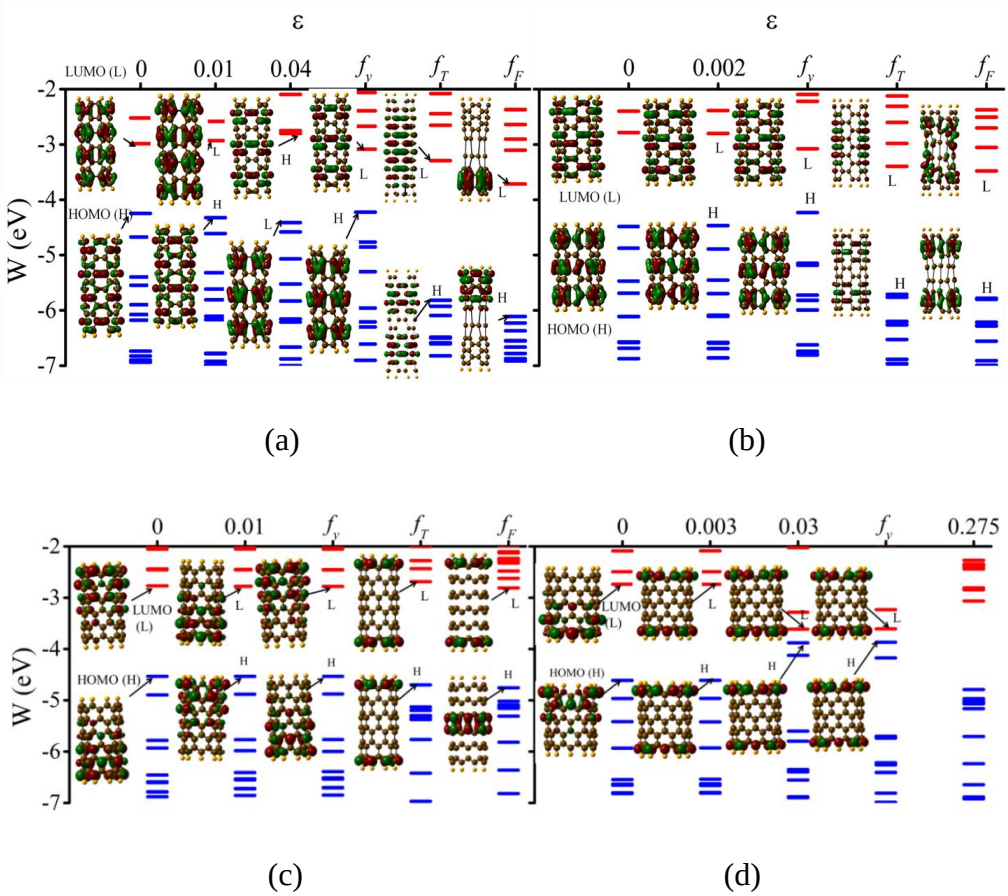

Figure 10. Molecular orbital spectra. Red and blue regions are occupied and unoccupied molecular orbitals of (a) CNT (4, 4), (b) CNT (5, 5), (c) CNT (8,0), (d) CNT(10,0) and (e) CNT (6,2).

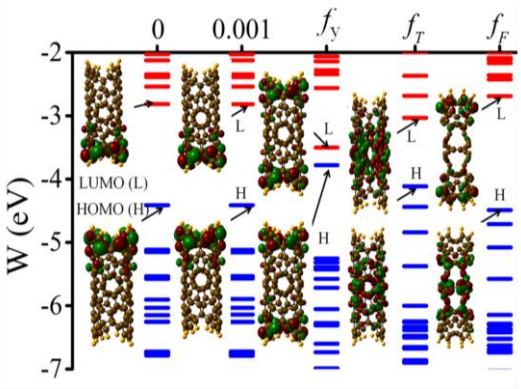

(e)

Figure 10. Continued.

Plastic deformation leads to the breaking of the delocalized orbitals; HOMO and LUMO localize according to the formed carbon-carbon bonds and their HLGs at f_y decrease from 1.26 to 1.14 eV, and from 1.70 to 1.15 eV for CNT(4,4) and CNT(5,5), respectively. At f_T, there is a breaking of the π-bonds of the CNT (n, n); the HOMO is on top of the CNT and then, loss of the π-bonds takes place once the necking starts. At f_T, the HLGs increase up to 2.52 and 2.31 eV for CNT (4,4) and CNT (5,5), respectively. At fracture (f_F), CNT (4,4) HOMO is localized at the bottom of the nanotube while the LUMO is localized at the top of it. The CNT (5,5) HOMO is delocalized in every cap formed at fracture.

On the other hand, zigzag HOMOs are partially delocalized and doubly degenerated. CNT (8, 0) HOMO is at the bottom of the nanotube, while CNT (10,0) HOMO is at the upper part. As the nanotube is pulled apart from 0 to 0.01, CNT (8,0) HOMO is located at the upper part of the nanotube, and after f_y, it migrates to the ends of the nanotube (Figure 10c). Nevertheless, when CNT (10,0) is stretched from 0.003 to f_y, its HOMO does not

change its position and it is always kept at the ends of the nanotubes. CNT (8,0) HOMO is localized in the middle part of the nanotube at the fracture point while its LUMO stays at the ends of the nanotube. CNT (6,2) HOMO stays in the upper part and its LUMO in the lower part of the nanotube from 0 to 0.001. However, when it reaches f_y, both HOMO and LUMO split into two parts and then they localize in the middle part of the nanotube at f_T. Finally, at f_F, CNT (6,2) HOMO and LUMO are localized in the two helical carbon chains and caps as it is observed in Figure 10(e). Consequently, the relation between mechanical and electronic properties reveals that carbon nanotubes that are stretched and deformed up to their tensile strength can be suitable materials for the fabrication of solar cells with absorptions in the range of 1.26-2.52 eV as deduced from the calculated HOMO-LUMO gaps. Also, because of the coupling of mechanical and electrical properties, it may be possible to control the adsorption of solar light from low to high energy by manipulating the stretching of the nanotubes.

Table 4. HOMO-LUMO gaps (HLG) of CNTs for the three points of the elastic region (HLG_n with n = 0, 1, 2), as well as for the yield strength (HLG_{fy}), tensile strength (HLG_{fT}), and fracture (HLG_F).

CNT	HLG_0	HLG_1	HLG_2	HLG_{fy}	HLG_{fT}	HLG_F
(4,4)	1.26	1.39	1.61	1.14	2.52	2.40
(5,5)	1.70	1.67	--	1.15	2.31	2.30
(8,0)	1.76	1.76	--	1.75	2.01	1.95
(10,0)	1.87	1.87	1.84	0.27	1.73	1.73
(6,2)	1.60	1.60	--	0.28	1.08	1.80

CHAPTER IV

Li-ION BATTERIES

4.1 Literature Review

As it was discussed earlier in chapter I, section 1.3, a layer called SEI is formed during charging in Li-Ion Batteries and this layer may diminish the battery performance. Thus, research is been conducted in order to understand the dependence of battery capacity with SEI. Peled[76] reported that to increase the cycle life of the batteries, a stable SEI has to be formed on the anode. An desirable SEI should have low electron conductivity, high Li+ conductivity, homogenous composition, and morphology.[17] Arreaga-Salas et al.[77] found that SEI is formed by lithium fluoride (LiF), Li_xPF_y and PF_y. Researchers have made efforts to find out ways to stabilize SEI; for example, it has been found that when a solvent like fluoroethylene carbonate (FEC) is added to the electrolyte, a more stable SEI is acquired and the capacity retention is enhanced in silicon electrodes.[78] [79] Ryu et al.[80] demonstrated that the passivation of the silicon electrodes with alkoxy silane functional groups improves the cycle life. SEI can be also stabilized by designing proper electrodes; for instance, Wu et al.[81] designed an anode using silicon nanotube which is wrapped with silicon oxide (Ion permeable) and found that the capacity of the anode is ameliorated with a capacity retention of 85% of their initial capacity after 6000 cycles. Liu et al.[82] fabricated a yolk-shell made of a silicon nanoparticle surrounded by a carbon shell and found that SEI is stable on the carbon surface due to the particle has the freedom to swell without breaking the carbon shell. Budi et al. found that LiF is the first chemical product

formed by the decomposition of the electrolyte followed by the Li_2F, then LiO and Li_2O using molecular dynamics simulations.[83]

Silicon has been proposed to be used as anode in lithium-ion batteries because silicon-lithium has theoretically a higher specific capacity of 4212 $mAhg^{-1}$,[84] than graphite (372 $mAhg^{-1}$)[77] and silicon is the second most abundant element on earth that can form mixtures with up to 4.4 lithium atoms/silicon atom ($Li_{4.4}Si$).[85] However, $Li_{4.4}Si$ expands 300% in volume during lithiation (intercalation of lithium atoms into silicon during charging) leading to change in the surface area and mechanical stresses.[86 87] Low cycling stability of the bulk silicon has impeded to commercialize successfully silicon lithium batteries[88] because the expansion of silicon during lithiation yield to poor battery capacity[89] and pulverization of the anode due to the internal stresses. However, one of the strategies used to solve this problem is to use nanostructured anode because these structures have short ion diffusion pathway and higher power rate in the electrochemical reactions.[90] These nanostructures also minimize the volume expansion, reduce the internal stresses by increasing the surface area and enhance the electrical conductivity of silicon.[91 92]

In this report, we investigate the current voltage characteristics of silicon-lithium nanostructured anodes, solid electrolyte interphase (SEI), and electrolyte using the combination of ab initio density functional theory and Green's function formalism.

4.2 Methodology

$Li_{4n}Si_n$ molecular structures are optimized until a minimum of energy using the B3PW91/6-31G(*d)* level of theory.[93] These structures are ended with gold atoms and re-optimized. LiF, Li_2O, Li_2CO_3, and $C_3H_4O_3$ (SEI) molecules are optimized and sandwiched between Li_8Si_2 (anode) and one gold atom (cathode). Then, external electric dipole fields are applied to the Li_8Si_2-SEI-Au molecular junctions. All these calculations are carried out using the program Gaussian 09.[22] Next, current-voltage (*I-V*) characteristics are obtained using Green's function formalism with the help of the generalized electron nanointerface program (GENIP).[94] This computational method has been used before to obtain *I-V* characteristics of polypeptides in alpha-helix conformation,[95] nanosensors in fissile materials,[96] and cobalt phthalocyanine complexes,[21] among others.

The calculations of the Li_8Si_2-SEI-Au molecular junctions with applied electric fields are done using B3PW91 method with basis sets: LANL2DZ and 6-31G(d). LANL2DZ[20] (los Alamos National Laboratory basis) is used for Au and Si; the 6-31G(d) [21 22] is used for Li, O, F, C, and H atoms. LANL2[20 23] effective core potentials are employed for Au. The density of states of gold is calculated using the CRYSTAL program.[24]

4.3 Nanostructured Anodes

Figure 11 shows the optimized molecular structures of the $Li_{4n}Si_n$ anodes from n=2-6 with gold atoms added at the end of the structures. After optimization, gold atoms are attached to two or three lithium atoms. The total energy for the singlet and some triplet states of

these structures are shown in Table 5. As a rule of thumb, structures with lowest energy are chosen to obtain the current-voltage characteristics (I-V). I-V of Si_nLi_{4n} structures yield symmetric curves and the largest current is obtained for Li_8Si_2 (I=314.08 μA at 5V). As the thickness of $Li_{4n}Si_n$ increases from 7.6Å to 22.8 Å, the electrical current decreases exponentially as shown in Figure 12(b). Then, Li_8Si_2 is chosen as a molecular structure to study the interaction between the anode, SEI, and electrolyte.

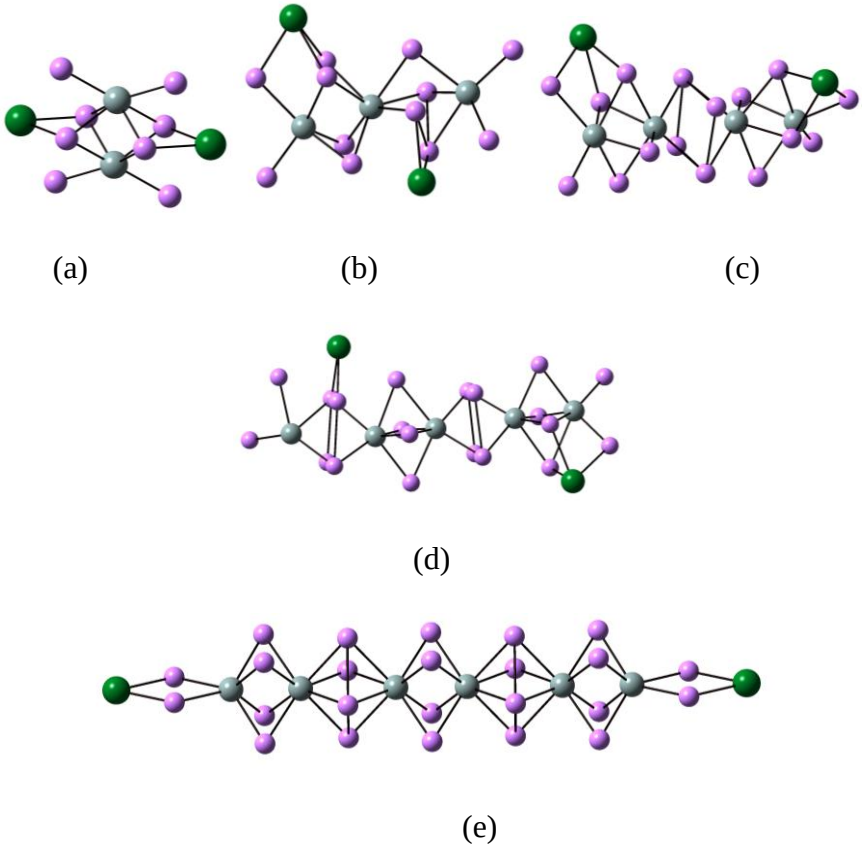

Figure 11. Silicon-lithium nanoelectrodes attached to gold atoms: (a) Li8Si2Au2, (b) Li12Si3Au2, (c) Li16Si4 and (d) Li20Si5 and (e) Li24Si6. Atom color code: Li (pink), Si (gray), Au (green).

Table 5. Energies of the $Li_{4n}Si_n$ with n=2-6, Li_8Si_2-$(MX)_l$-Au_2 with MX= Li_2O, LiF and Li_2CO_3 molecules, and Si_2Li_8-$(MX)_m$-EC-Au_2 where EC is ethylene carbonate and l=1,2,3. m is the multiciplity and it can either singlet or triplet. * $(Li_2O)_n$ are optimized.

$Li_{4n}Si_n$	m	Energy	$Li_{4n}Si_n$	m	Energy
$Li_8Si_2Au_2$	1	-910.32437	Li_8Si_2-$(Li_2O)_3$-Au_2	1	-1181.0156
	3	-910.29831	Li_8Si_2-LiF-Au_2	1	-1017.6409
$Li_{12}Si_3Au_2$	1	-1229.9014		3	-1017.6082
	3	-1229.8683	Li_8Si_2-$(LiF)_2$-Au_2	1	-1125.0178
$Li_{16}Si_4Au_2$	1	-1549.4993	Li_8Si_2-$(LiF)_3$-Au_2	1	-1232.4042
	3	-1549.4907	Li_8Si_2-Li_2O-EC-Au_2	1	-1342.7539
$Li_2Si_{50}Au_2$	1	-1869.0887	Li_8Si_2-$(Li_2O)_2$-EC-Au_2	1	-1433.0097
$Li_{24}Si_6Au_2$	1	-2188.6791	Li_8Si_2-$(Li_2O)_3$-EC-Au_2	1	-1523.2636
Li_8Si_2-Li_2O-Au_2	1	-1000.5223	Li_8Si_2-Li_2CO_3-EC-Au_2	1	-1531.3705
Li_8Si_2-Li_2O-LiF-Au_2	1	-1107.8944	Li_8Si_2-$(Li_2CO_3)_2$-EC-Au_2	1	-1810.2531
	3	-1107.8684	Li_8Si_2-$(Li_2CO_3)_3$-EC-Au_2	1	-2089.1402
Li_8Si_2-Li_2O-LiF-Li_2O-Au_2	1	-1198.1497	Li_8Si_2-$(Li_2O)_2$-EC-Au_2*	1	-1433.0931
	3	-1198.128	Li_8Si_2-$(Li_2O)_3$-EC-Au_2*	1	-1523.442
Li_8Si_2-$(Li_2O)_2$-Au_2	1	-1090.7694			

4.4 Electrical Properties

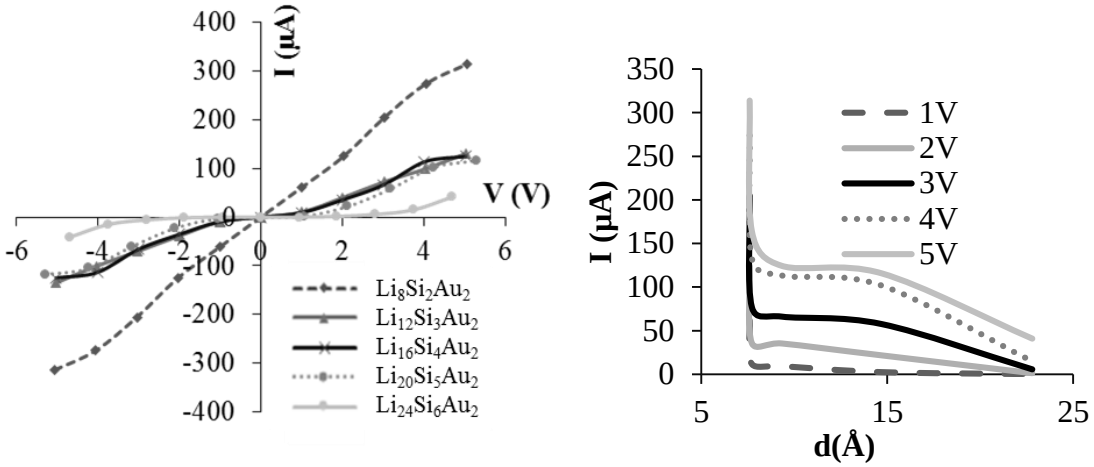

(a) (b)

Figure 12. Current (I) versus voltage (V) of Li4nSin nanoelectrodes with n = 2-6, and (b) current versus thickness (d) of Li4nSin at voltages from 1 to 5V.

Although SEI is conformed of different molecules that are produced from electrochemical reactions, Li_2O, LiF, and Li_2CO_3 are selected to represent a piece of SEI and simulate the SEI's behavior; these molecules are simulated initially as not bonded to simulate the first stages of the nucleation process (molecules that will form the new phase). This is done by taking the distance between outer atoms 5% higher than the sum of the Van der Waals radius of these atoms. Different combinations of these molecules and compositions are used to simulate a piece of SEI and investigate the electron transport in Li_8Si_2 anodes with a SEI layer. The first studied cases are the Li_8Si_2-Li_2O, Li_8Si_2-Li_2O-LiF, and Li_8Si_2-Li_2O-LiF-Li_2O and their I-Vs are shown in Figure 14(a, c, e).

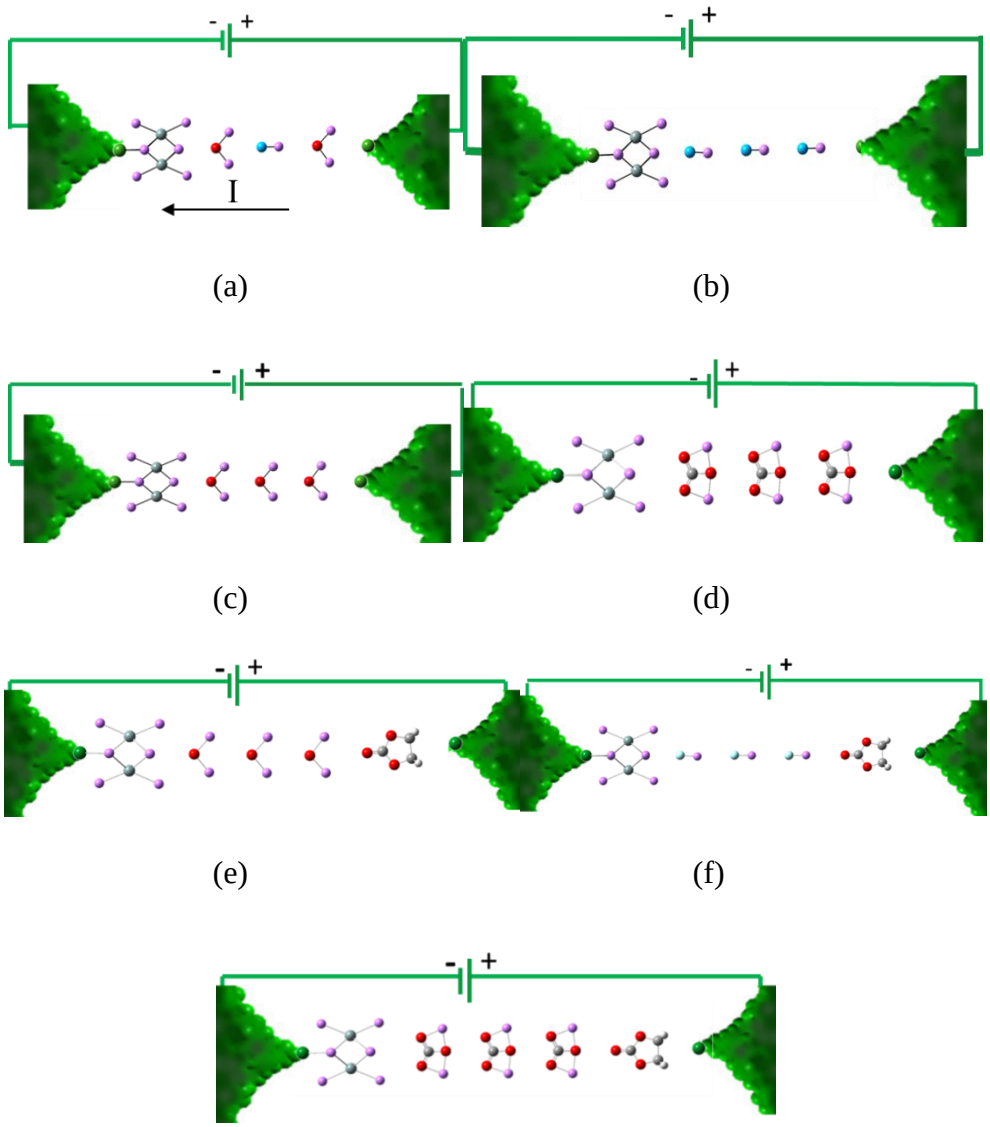

Figure 13. Molecular junctions of (a) Li_8Si_2-Li_2O-LiF-Li_2O, (b) Li_8Si_2-$(LiF)_3$, (c) Li_8Si_2-$(Li_2O)_3$, (d) Li_8Si_2-$(Li_2CO_3)_3$ (e) Li_8Si_2-$(Li_2O)_3$-EC (f) Li_8Si_2-$(LiF)_3$-EC and (g) Li_8Si_2-$(Li_2CO_3)_3$-EC. SEI is Li_2O, LiF, Li_2CO_3, and the electrolyte is $C_3H_4O_3$.

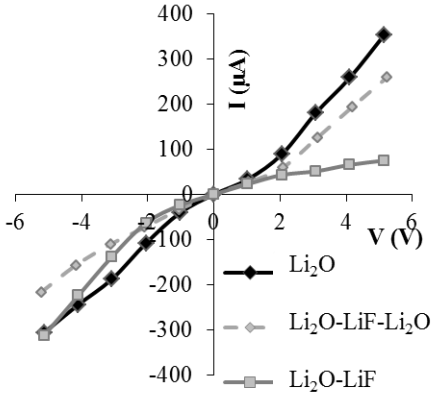

(a)

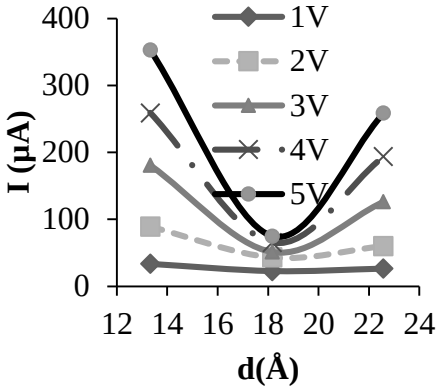

(b)

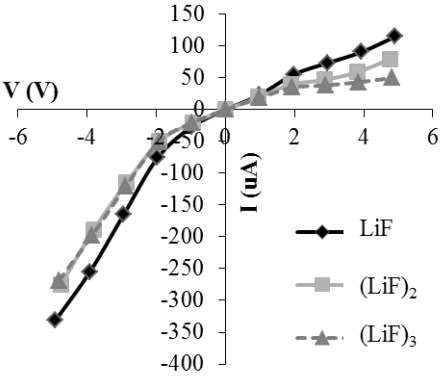

(b)

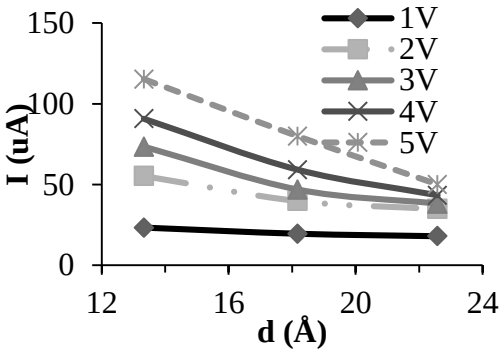

(d)

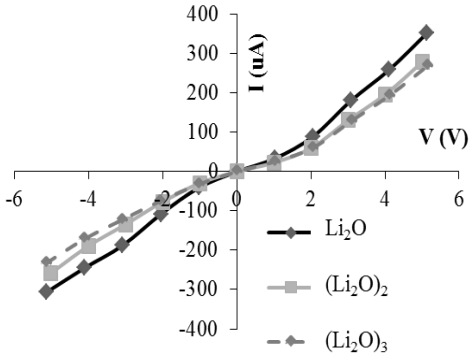

(e)

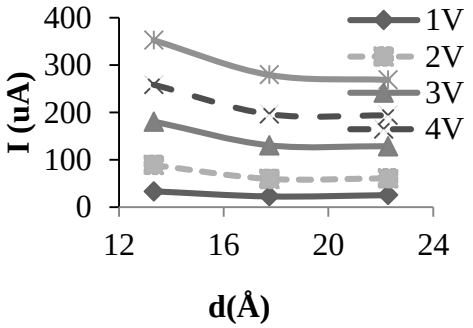

(f)

Figure 14. Current-voltage (I-V) characteristics of (a) Li8Si2-Li2O, Li8Si2-Li2O-LiF, Li_8Si_2-Li_2O-LiF-Li_2O, (c) Li_8Si_2-$(LiF)_n$, (e) Li_8Si_2-$(L_2O)_n$ with n=1,2,3. Current (I) versus SEI thickness (b) Li_8Si_2-Li_2O-LiF-Li_2O (d) Li_8Si_2-$(LiF)_n$ (f) Li_8Si_2-$(L_2O)_n$.

Larger currents are obtained for Li_8Si_2-Li_2O than Li_8Si_2-Li_2O-LiF and Li_8Si_2-Li_2O-LiF-Li_2O. Surprising, larger currents are obtained for Li_8Si_2-Li_2O-LiF-Li_2O than Li_8Si_2-Li_2O-LiF. Better electron transport is obtained when SEI is composed mainly of Li_2O than LiF. This statement can be corroborated in Figure 14(c and e) where smaller currents are calculated for LiF (115.22 μA) than Li_2O (353 μA) at 5V. As the thickness of LiF increases, lower currents are obtained as portrayed in Figure 14(d) and the electron transport in LiF decreases with SEI thickness more rapidly than in Li_2O during the nucleation process.

Then, a piece of SEI layer formed of LiF blocks the electron transport to the anode (Li_8Si_2) as its thickness increases. This behavior can also be explained with the help of the molecular electrostatic potentials (MEP) that are displayed in Figure 15, the red and blue sections are potentials formed due to electrons and neutrons, respectively. Negative potentials are found in the direction of the applied electric field for (Li_2O) with n = 1 and 3 (Figure 15a-b). Different molecular electrostatic potentials are obtained for LiF than Li_2O therefore is expected that different electrical currents are calculated for Li_2O than LiF. When LiF is present in the SEI, the conduction path is formed by an alternation of the negative and positive potentials (Figure 15e). This alternated potential hampers the electron mobility from the anode to the electrolyte during charging and lower electron transport is obtained compared to Li_2O. These preliminary results shows that less electrons are escaping from the anode during charging when SEI is formed of LiF, which is translated in an increase of cation conductivity from the electrolyte to the anode.

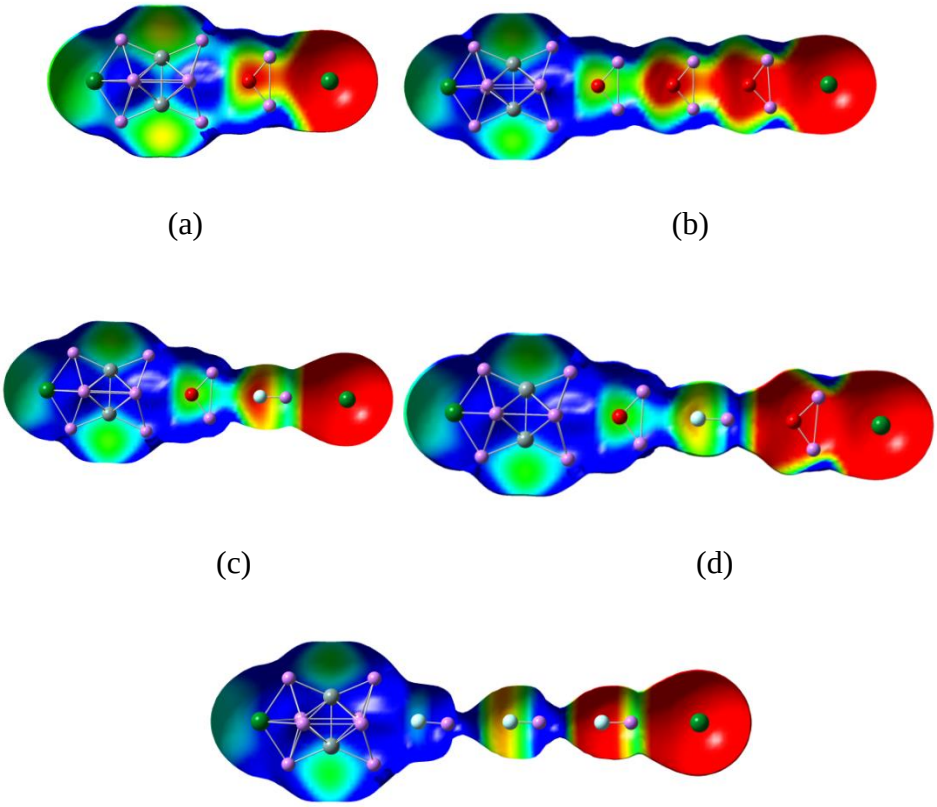

Figure 15. Molecular electrostatic potentials (MEP) of (a) Au-Li_2Si_8-Li_2O-Au, (b) Au-Li_2Si_8-$(Li_2O)_3$-Au, (c) Au-Li_2Si_8-Li_2O-LiF-Au, (d) Au-Li_2Si_8-Li_2O-LiF-Li_2O-Au, and (e) Au-Li_2Si_8-$(LiF)_3$-Au.

Second, the I-V characteristics of Li_8Si_2 (anode), SEI and electrolyte are analyzed. A molecule of ethylene carbonate (EC) is chosen to represent the electrolyte which is mainly composed of alkyl carbonates.[97] IVs characteristics indicate that the electrical current does not change neither with the composition or thickness of SEI when EC is present. Therefore, the electron transport is independent of SEI thickness as displayed in Figure

16b, d, and f. This can be explained with the help of the molecular orbitals spectra that are shown in Figure 17. First, larger currents (1140μA at 5V) are calculated due to small HOMO-LUMO (H-L) gaps (0.14eV-0.26eV, Table 6) and this H-L gap does not change significantly as the thickness of SEI increases; for example, for Li_2O, the H-L=0.26 eV, $(Li_2O)_2$ the H-L=0.18eV and $(Li_2O)_3$ the H-L=0.14eV.

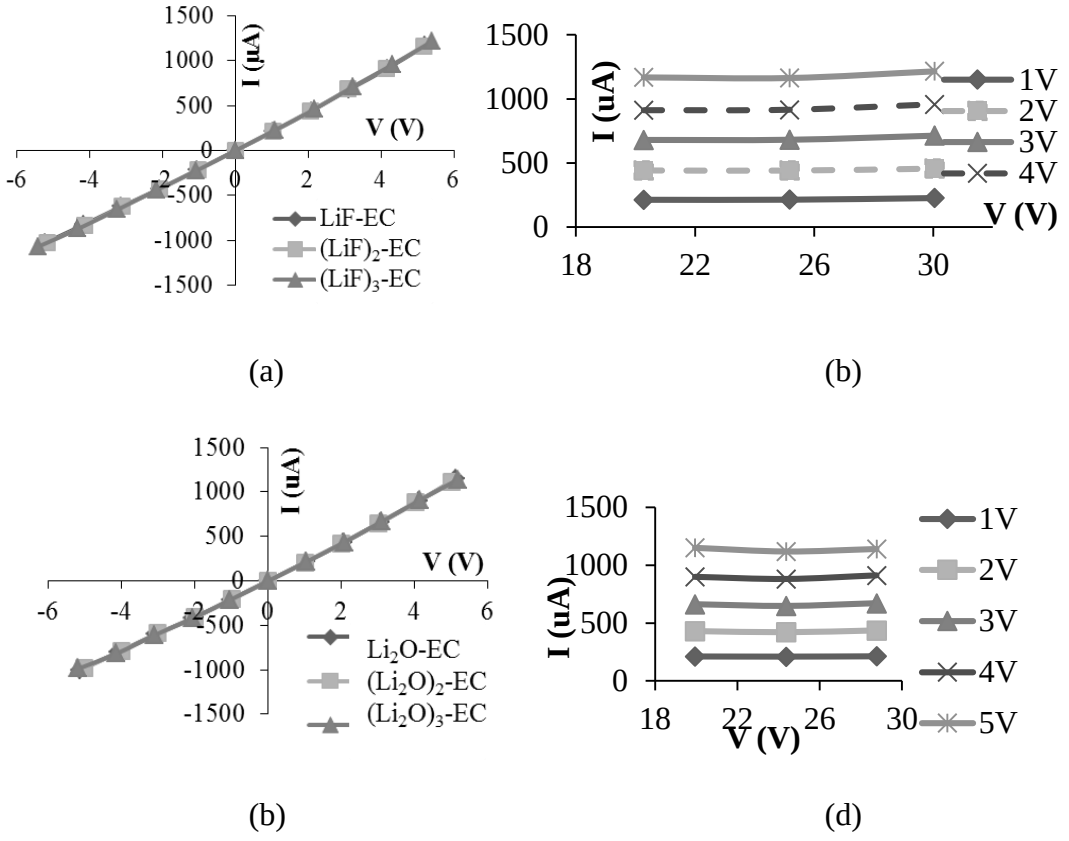

Figure 16. Current-Voltage (I-V) of (a) Li_8Si_2-(LiF)n-EC, (c) Li_8Si_2-(Li_2O)n-EC, and (e) Li_8Si_2-(Li_2CO_3)n. Electrical current (I) versus SEI thickness (d) of (b) Li_8Si_2-$(LiF)_n$-EC (d) Li_8Si_2-(Li_2O)n-EC (e) Li_8Si_2-$(Li_2CO_3)_n$ with n=1,2,3. EC is ethylene carbonate.

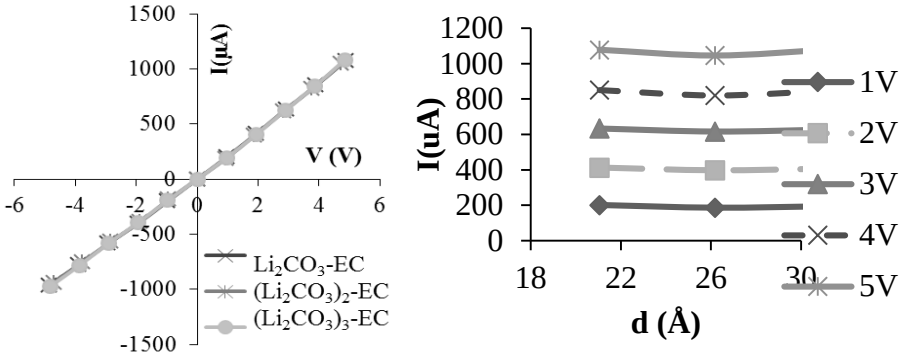

(e) (f)

Figure 16. Continued.

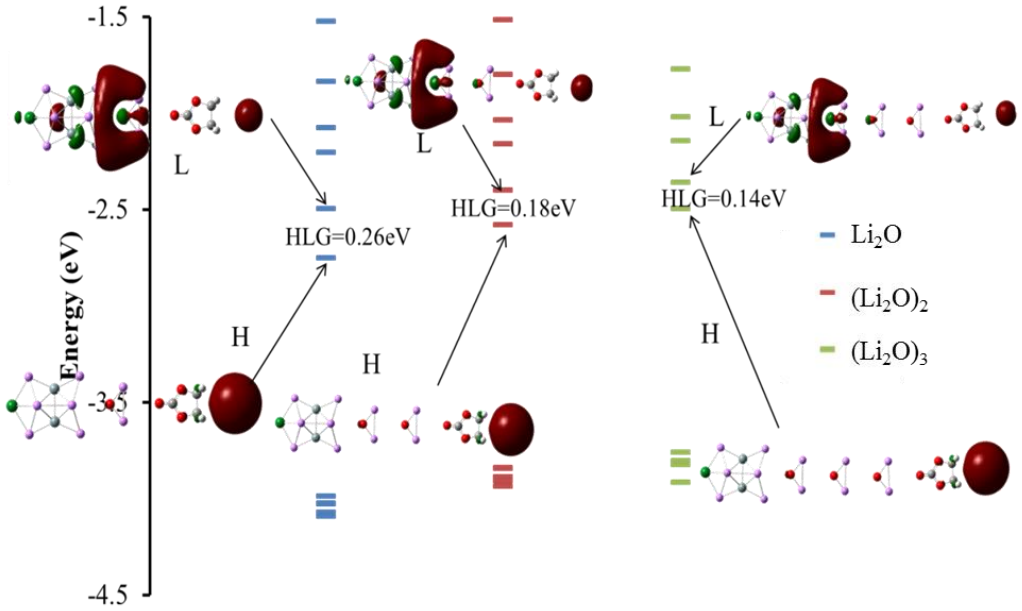

(a)

Figure 17. Molecular orbital spectra of (a) Li_8Si_2-$(Li_2O)_n$-EC and (b) Li_8Si_2-$(LiF)_n$-EC with n=1,2,3.

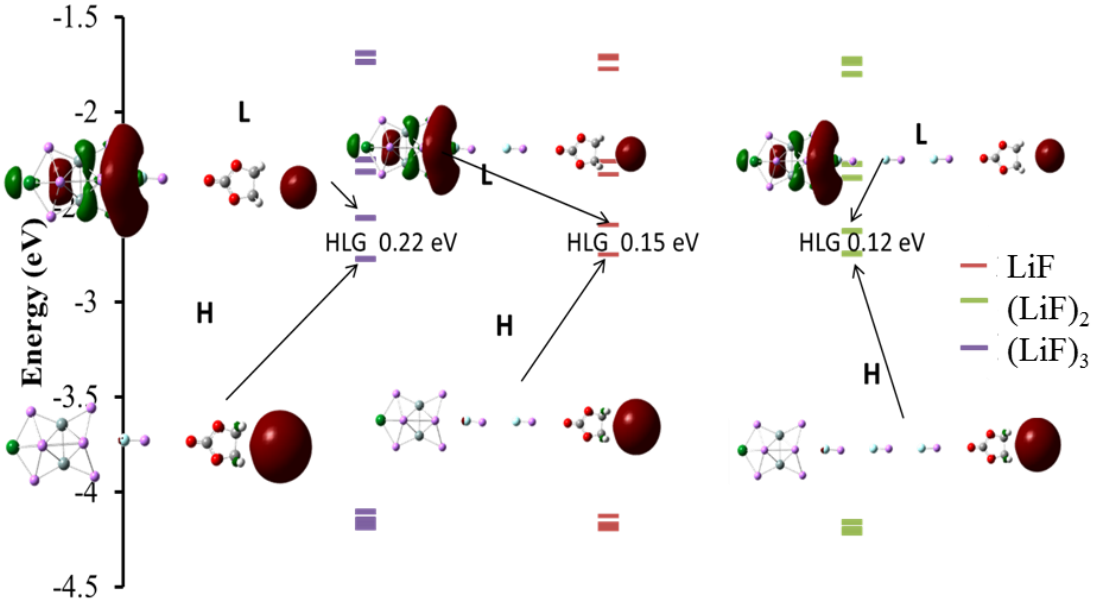

(b)

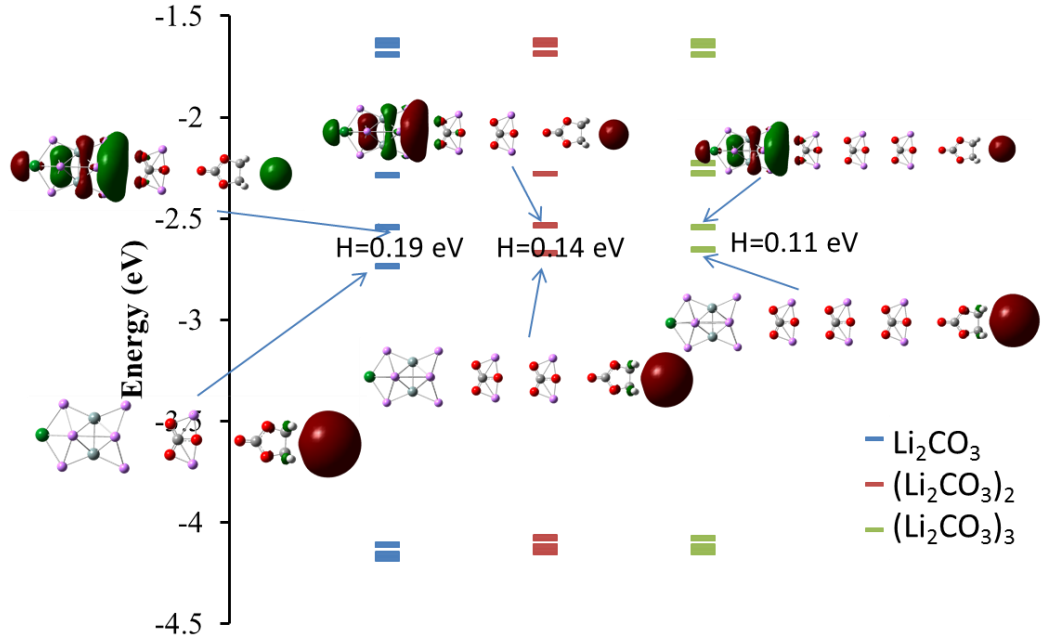

(c)

Figure 17. Continued.

Table 6. HOMO (H) and LUMO (L) energies with their respective HOMO-LUMO gap (HLG). All the energies are in eV.

$(Li_2O)_n$	H	L	HLG	$(LiF)_n$	H	L	HLG
Li2O	-2.75	-2.50	0.26	LiF	-2.78	-2.56	0.22
$(Li_2O)_2$	-2.58	-2.40	0.18	$(LiF)_2$	-2.75	-2.60	0.15
$(Li_2O)_3$	-2.50	-2.36	0.14	$(LiF)_3$	-2.75	-2.63	0.12

Even, the HOMO shape does not change as the SEI (LiF or Li_2O) molecules vary due to the localization on one of the gold atoms. Figure 18 shows the transmission functions and density of states spectra of Li_2Si_8-(Li_2O)-EC, Li_2Si_8-$(LiF)_n$-EC, and Li_2Si_8-$(Li_2CO_3)_n$-EC . The electron transport is dependent in the transmission function (TF), and in Li_2Si_8-SEI-EC structures does not improve as the thickness of SEI increases because the TFs do not change around the Fermi level and the frontier orbitals (HOMO and LUMO) (dotted squares in Figure 18).

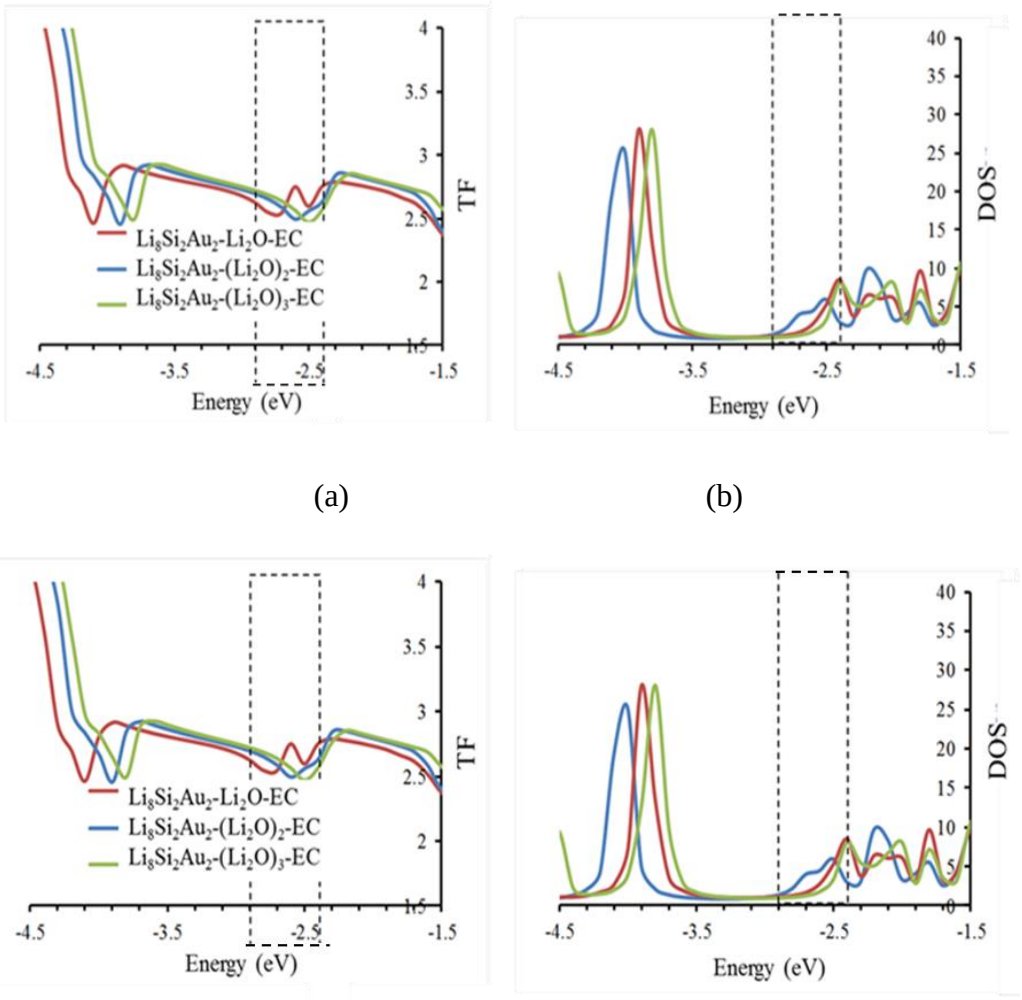

Figure 18. Transmission function (TF) and density of states (DOS) of (a),(b) Li_8Si_2-(Li_2O)n-EC and (c), (d) Li_8Si_2-(LiF)n-EC and (e), (f) Li_8Si_2-$(Li_2CO_3)_n$-EC with n=1,2,3, respectively.

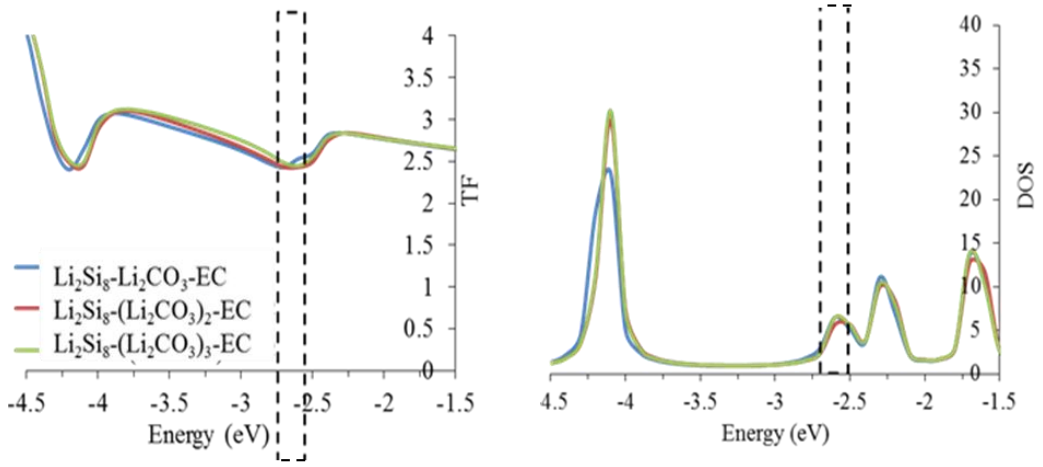

(e) (f)

Figure 18. Continued.

MEP of Li_2Si_8-SEI-EC shows that EC has a negative electrostatic potential which behaves as an ion conduction path for Li^+, this path becomes less negative when it approaches to the SEI regions as is shown in Figure 19. MEPs are excellent tools to visualize how SEI blocks the ion conductivity in Li-Ion Batteries. SEI has a less negative electrostatic potential when is composed mainly of LiF. In order to know the possible explanation of non-change in the I-Vs when EC is present, $(Li_2O)_n$ with n=1-4 are optimized, and simulate them as bonded, the optimization yield that one of the Li_2O molecules is twisted perpendicular to the plane as shown in Figure 20.

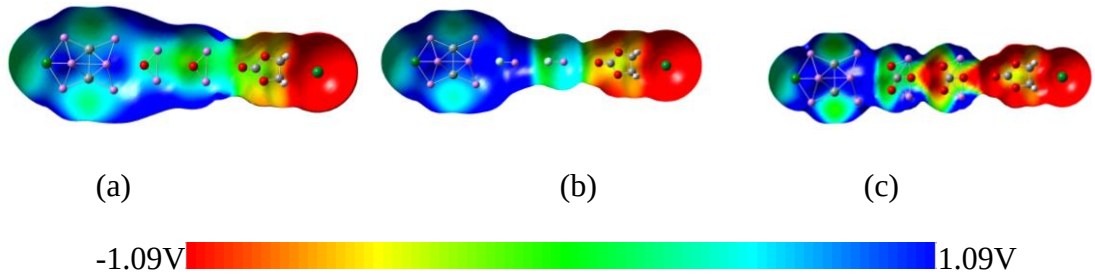

Figure 19. Molecular electrostatic potentials of (a) Li_2Si_8-$(Li_2O)_2$-EC, (b) Li_2Si_8-$(LiF)_2$-EC, and (c) Li_2Si_8-$(Li_2CO_3)_2$-EC. EC is the ethylene carbonate.

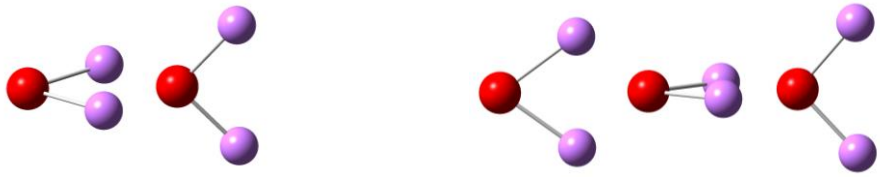

Figure 20. Optimized molecular structure of (a) $(Li_2O)_2$ and (b) $(Li_2O)_3$. One of the Li_2O is rotated perpendicular to the plane of this document.

Optimized $(Li_2O)_n$ are sandwiched between Au-Li_8Si_2 and EC-Au and I-V characteristics are calculated. There is a variation in the electrical current when Li_2O are bonded despite that EC is present and larger currents are obtained for anode-$(Li_2O)_3$-EC than anode-$(Li_2O)_2$-EC as shown in Figure 21. Lower currents are obtained for even number of Li_2O than odd and it seems that the rotation of the Li_2O and the number of these molecules play a role in the electron transport in Li-Ion Batteries.

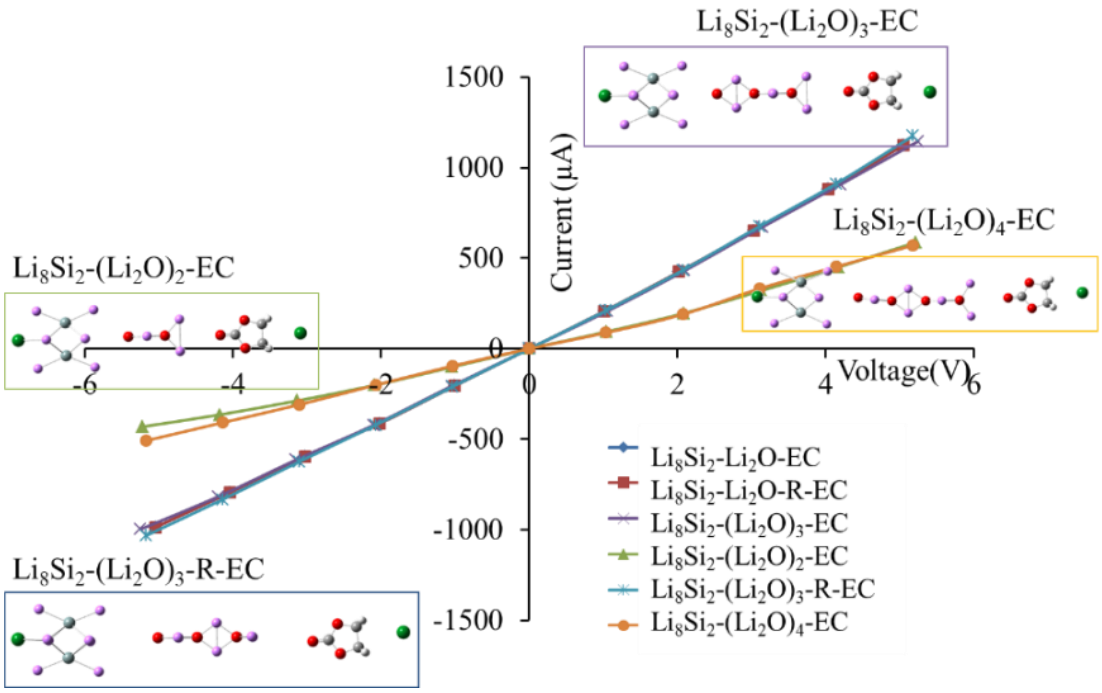

Figure 21. Current-Voltage characteristics of optimized $(Li_2O)_n$ with n=1,2,3,4 sandwiched between Au-Li_8Si_2 and EC-Au. EC is ethylene carbonate, R means that Li_2O molecules where rotated 90º.

4.5 Recommendations

Due to the importance of developing batteries for multiple applications, further research need to be carried out in this area. The results of the research presented in this document show that LiF has lower electron conductivity than Li_2O and Li_2CO_3 and also the MEPs show the positive electrostatic potential around SEI when it is composed of LiF which may restrict Li+ mobility. For this reason, it is recommended to study the reduction reactions when SEI is formed and identify the reaction that yields LiF in order to control the concentration of this compound because its presence in the SEI affects the ion mobility.

CHAPTER V

DEGRADATION OF POLYVINYL ALCOHOL UNDER MECHANOTHERMAL STRETCHING*

5.1 Polyvinyl Alcohol

A polymer is a large molecule with a carbon backbone, conformed of several monomers (repeat units). The backbone have side chains or groups which lead to different chemical and mechanical properties due to the different bonds (Van der Waals) that can be formed between the chains. Polyvinyl alcohol (PVA) is an atactic polymer, has alcoholic groups along the chain, and is water soluble. PVA interacts with other molecules through hydrogen bonding, cross-linking, and oxidation.

PVA has extensive applications such as adhesives,[84] textile sizing,[77] surfactants,[85] membranes for sound absorption,[86] emulsifiers, oil resistant, and several others. PVA's melting temperature is 230 °C and degrades rapidly above 200 °C.

5.2 Literature Review

Mechanical forces have significant effects on the behaviors of materials. A mechanical force can induce the oxidation of metals[12, 14, 78, 98] and alter the electron pathways of an organic molecule. Understanding the mechanisms of mechano-activated chemical

---

* This chapter is reprinted with permission from:
Degradation of Polyvinyl Alcohol under Mechanothermal Stretching, by D. Cristancho et al., 2013. J. Mol. Model. 19: 3245-3253. Copyright 2013 by Springer-Verlag Berlin Heidelberg.

reactions are the key to obtain control and precise predictions of materials. Besides mechanical activation, thermal energy also affects the behaviors of materials.[77] Mechanical properties of polymers can be improved by using cross-linking reactions. Cross-linked polymers are used in medical implants because their low cytotoxicity and high biocompatibility.[87] Cross-linking in polymers can be achieved by radiation exposure such as electron beam,[88] gamma radiation,[89] and X-ray radiation.[90]

Akhter et al. reported the first X-ray photoelectron spectroscopy (XPS) analysis of PVA. Three degradation routes have been found: cross-linking to form an ether group, oxidation to form a carbonyl group, and oxidative-induced chain-scission to form a carboxylated group.[91] Beamson et al. reported that the initial rate of the degradation of PVA varied linearly with X-ray intensity. The C-O functional groups were broken during PVA degradation which created a blend of polymers with functionalities such as CH_2-CO_2R_1, CH_2, C=O, and CO_2R_2.[92]

Molecular orbital energies of core electrons are alike with the binding energies from XPS. When a sample surface is irradiated with X-rays, the core electrons are ejected if enough energy is provided to ionize them. Thus the molecular orbital energies can be obtained experimentally and theoretically. In the analysis of XPS spectra, the carbon peaks are commonly used as the calibrating references. However, the reliability of such references is an issue when the samples are under mechano-thermal stretching. Here we investigate the chemistry of PVA that was coated on a lead sheet with dispersed tantalum powder

(Figure 22). Lead's thermal expansion coefficient is one of the highest among metallic elements. By using in situ heating, lead provided the mechanical stretching that worked together with the thermal expansion from PVA itself. Both high- and low-molecular weight PVA was characterized using XPS. The binding energies of different carbon species were analyzed using first principles quantum chemistry.

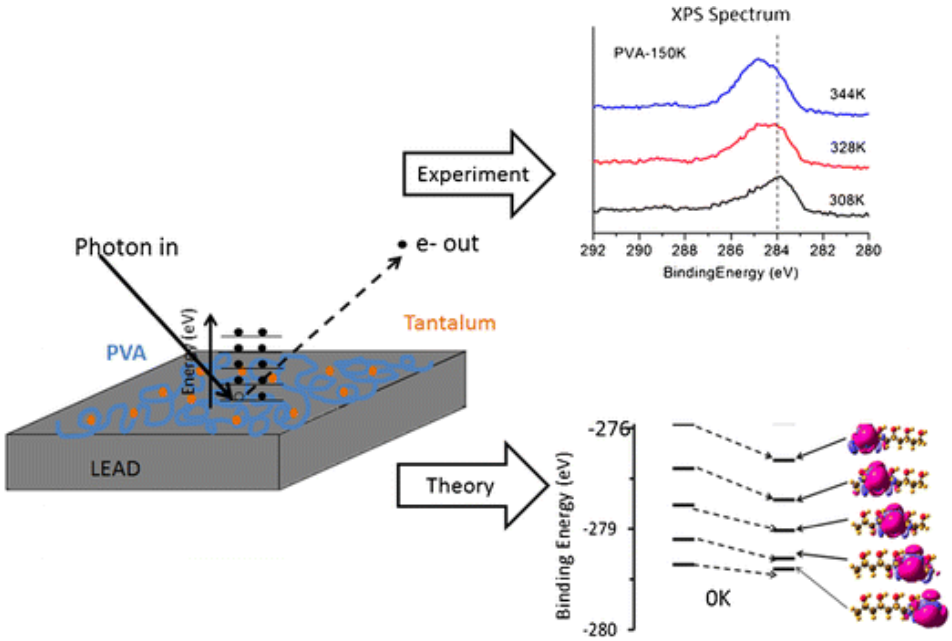

Figure 22. Degradation of PVA under mechano-thermal stretching using XPS and quantum mechanical calculations. Figure adapted from Cristancho et al.[99]

5.3 Methodology

5-mer polyvinyl alcohol with molecular structures, $C_{10}H_{22}O_5$, $C_{10}H_{19}O_5$, and $C_{10}H_{20}O_6$ (Figure 23a, b, d), are optimized until local minima are obtained. A second-derivative calculation is performed for each optimized structure to make sure that the optimized geometries correspond to local minima. Then, the carbon-carbon bonds lengths are

elongated 5% (to mimic the bond stretching produced by temperature changes), all other coordinates are constrained, and re-optimized leading to a structure called PVA-5. In order to validate the experimental data provided from XPS analysis, we use the DFT B3PW91 hybrid functional, which includes the Becke-3[22] exchange and the Perdew-Wang-91 correlation functional[94-95] as well as the Hartree-Fock (HF) method. All calculations are performed using the Gaussian 09 program.[96] The basis sets used are STO-nG (n = 3 and 6),[21, 30-31] 6-31G(d),[32, 97a] 3-21G(d),[97b, 100] and cc-pVDZ[101] to reproduce the values for the C(1S) binding energy (BE).

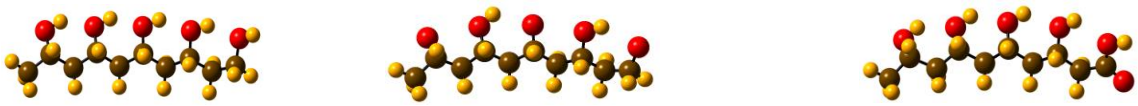

(a) (b) (c)

Figure 23. Polyvinyl alcohol (PVA) optimized structure, $C_{10}H_{22}O_5$, (b) PVA optimized structure with ketone groups, RC (=O) R, $C_{10}H_{19}O_5$ and (c) carboxyl group C-O at the end of the chain, $C_{10}H_{20}O_5$. C: brown, O: red, and H: yellow.

5.4 Results

The experimental results showed that the BE of PVA is molecular weight dependent. Figure 24 shows the XPS spectra of PVA-10k and PVA-150k. The BE of the major carbon peaks were around 285 eV, which matched the values reported in literature.[91, 102] For the major peaks in PVA-10k, there was a 0.2 eV BE increase when the temperature was changed from 310 K to 345 K. The increase was enlarged to 0.9 eV for PVA-150k. This increment in BE may be considered as a signature of polymer degradation through

oxidation. Once the chemical bond (C-O) is formed, the changes of the valence electron charge yield an increase in BE.

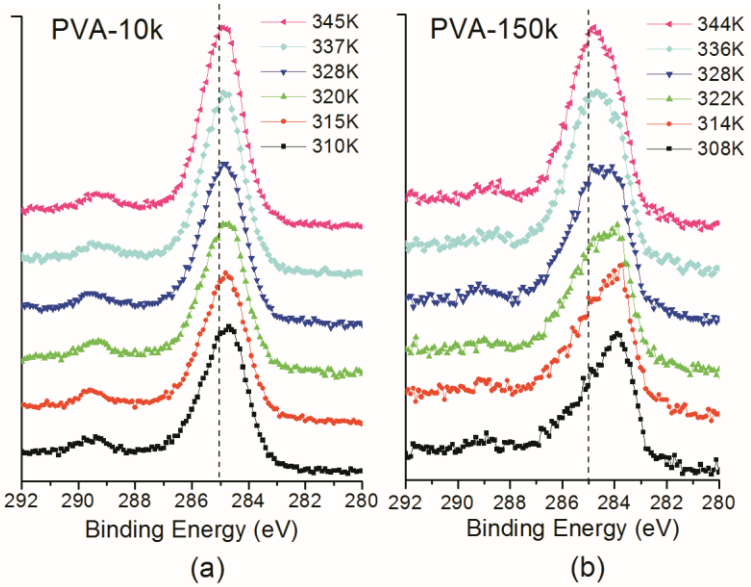

Figure 24. The XPS spectra of PVA-10k and PVA-150k as temperature increased from 310 K to 345 K (PVA-10k) and 308 K to 344 K (PVA-150k). (a) PVA-10k; (b) PVA-150k.

The carbon species from PVA-10k and PVA-150k were determined by the deconvolution process. As shown in Figure 25, four types of carbon species were found at low temperature for PVA-10k and PVA-150k: saturated hydrocarbon (C-H) at 284.6 eV and 283.8 eV, alcoholic group (C-O) at 285.6 eV and 285.2 eV, carbonyl group at 287.0 and 286.5 eV (C=O), and carboxylate group (O-C=O) at 289.5 eV and 288.8 eV. The presence of O-C=O and C=O shows that PVA samples were damaged by the sputtering process.

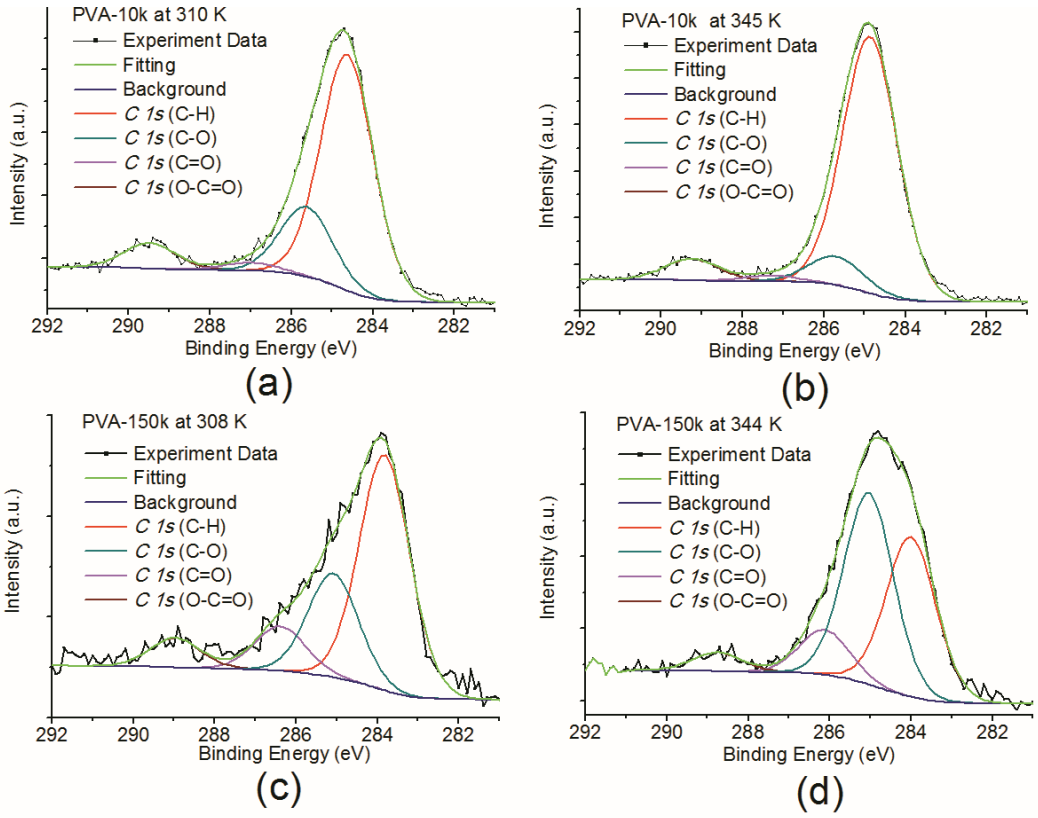

Figure 25. Deconvoluted C (1S) spectra of saturated hydrocarbon (C-H), alcoholic group (C-O), carbonyl group (C=O) and carboxylate group (O-C=O). (A) PVA-10k at 310 K; (B) PVA-10k at 345 K; (C) PVA-150k at 308 K; (D) PVA-150k at 344 K.

5.5 Degradation Mechanism

Thermal evolution results (Figure 26) suggest that the PVA samples chemically degraded at 308 K–345 K. PVA-10k and PVA-150k have different thermal degradation mechanism (Figure 27). PVA-10k: When the temperature was raised from 310 K to 345 K (Figure 26a), the concentration of C-C increased at the same rate that C-O decreased, leaving C=O and O-C=O species practically unchanged. This behavior may be attributed to the X-ray irradiation on a polymer of low molecular weight makes C-O bonds break, leaving C unbounded and ready to bind to the nearest C (polymerization by entanglement). H_2O_2

was generated as the by-product and decomposed to water and oxygen (Figure 27a). A different behavior was observed for PVA-150k. When the temperature was raised from 308 K to 345 K, the concentration of C-C decreased (depolymerization) at the same rate that C-O (cross-linked degradation (oxidation)) increased (Figure 26b); however the concentration of C=O was kept constant. Furthermore, another signature of oxidation was observed as the concentration of O-C=O species decreased when either C-O or C=O bonds could break, allowing the formation of C-O-C. This behavior suggests that a cross-linking reaction might happened once the temperature was raised, liberating H_2O as by-product of the reaction (Figure 27b). The resulting carbon species have the same BE been reported elsewhere.[92]

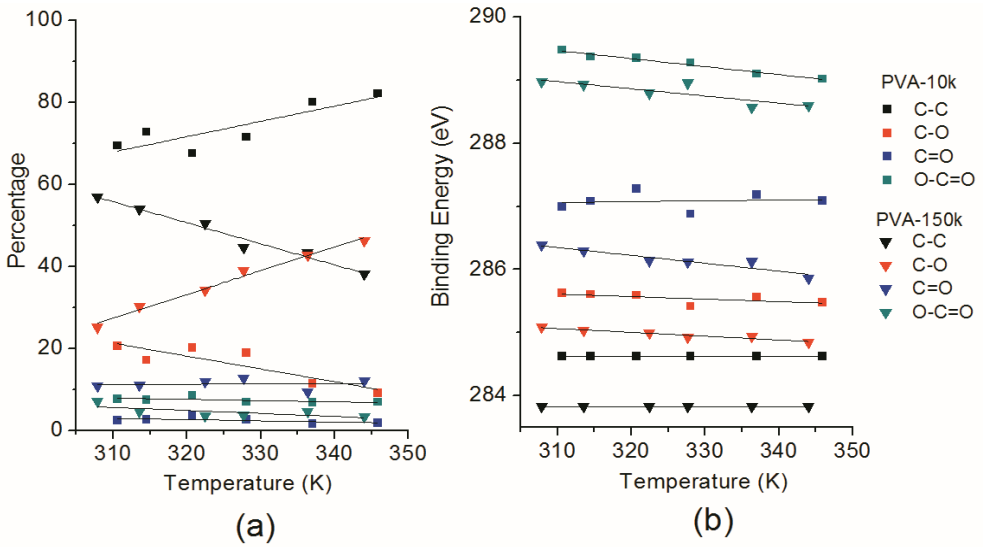

Figure 26. Composition (a) of carbon species versus temperature variation and their corresponding BE (b) calibrated with respect to the C-C.

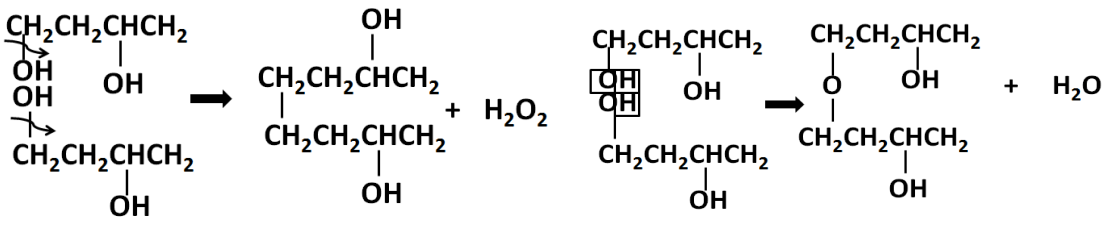

(a) (b)

Figure 27. Proposed degradation mechanism for PVA with low and high molecular weight. (a) Polymerization reaction for PVA-10k and (b) Cross-linking reaction for PVA-150k.

5.6 Computational Results

Experimental results suggest that thermal degradation of PVA is molecular weight dependent. With the purpose of validating and understanding this further, we carried out ab initio calculations. The sample surface is irradiated with X-rays, which hit the PVA core electrons. We assume a correlation between (1) the experimental core-electron BE shift when the sample's temperature is increased from 310-345 K and (2) the molecular orbital energy shift of core electrons from the PVA to the PVA-5. Figure 28 shows the molecular orbital energy for PVA (blue) and PVA-5(orange) and their corresponding shapes which are localized in the carbon atoms. When the C-C bond lengths of the PVA are elongated 5%, the calculated energy changes for the molecular orbitals localized in the C-O and C-C bond are in average 0.22 eV and 0.21 eV (B3PW91/6-31G(d)), respectively. The changes of energy matched with the changes in core-electron binding energy when the sample temperature rises from 310 to 345 K for PVA-10k. This suggests that the change in binding energy of 0.2 eV for PVA-10k is due to thermal stretching.

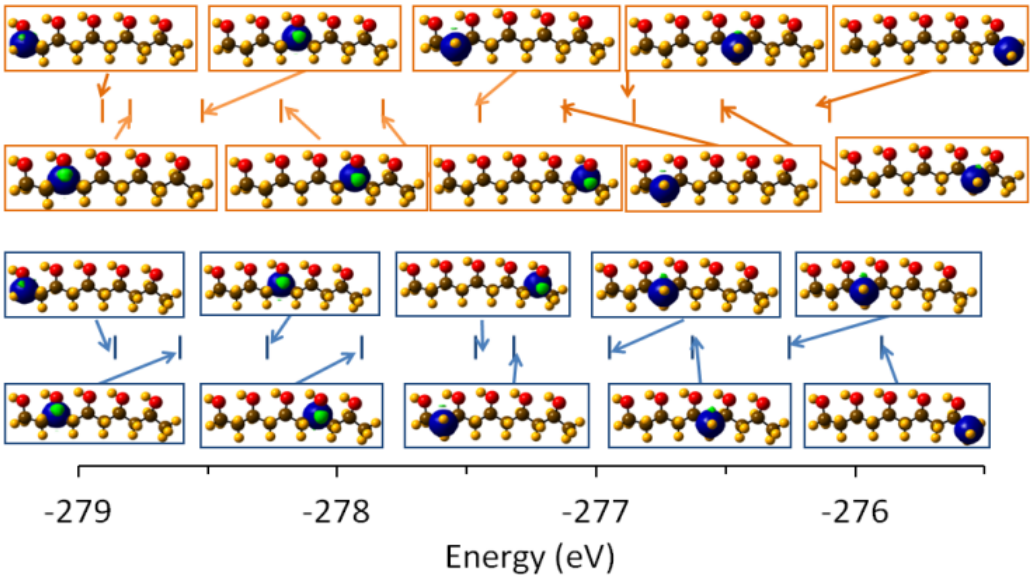

Figure 28. Molecular orbital energies for the unstretched (blue) and stretched by 5% in length (orange) of 5-mer polyvinyl alcohol using B3PW91/6-31G(d) level of theory.

Figure 28 shows the molecular orbitals energies and their corresponding shapes for PVA and PVA-5 using B3PW91/6-31G(d). Although this level of theory yields the best performance and is widely used in theoretical calculations,[103] it does not reproduce the absolute experimental BE of core electrons because this method is prepared mostly for the valence electrons. However, core electron energy trends are still acceptable. Therefore, we test the STO-3G, STO-6G, 6-31G(d), as well as the core-uncontracted n-31G(d) (n = 7, 10, 12, 16), and cc-pVDZ with B3PW91 functional.

Table 7. Change of core molecular orbital energies (ΔE) of PVA and PVA-5 for C-C and C-O using several level of theory.

Method	Basis-Set	ΔE (eV) C-C	ΔE (eV) C-O
B3PW91	STO-3G	0.07	0.09
B3PW91	STO-6G	0.16	0.14
B3PW91	6-31G(d)	0.23	0.20
B3PW91	7-31G(d)	0.23	0.21
B3PW91	10-31G(d)	0.08	0.14
B3PW91	12-31G(d)	0.23	0.20
B3PW91	16-31G(d)	0.23	0.20
B3PW91	cc-pVDZ	0.23	0.20
HF	10-31G(d)	0.13	0.19

We also use a 10-31(d) uncontracted core where the core-exponents are taken from the cc-pVDZ, producing a relatively large change in core energies; however, for all the others cases, the improvement of basis sets does not yield any variation in the core energies as shown in Figure 29. Therefore, HF and MP2 approaches are tested using the basis sets 6-31G(d), STO-3G and 10-31G(d). The best results are obtained for the uncontracted HF/10-31G (d) (dashed square) HF and MP2 approaches are tested using basis set STO-3G and HF/n-31G(d) (n = 6, 10)

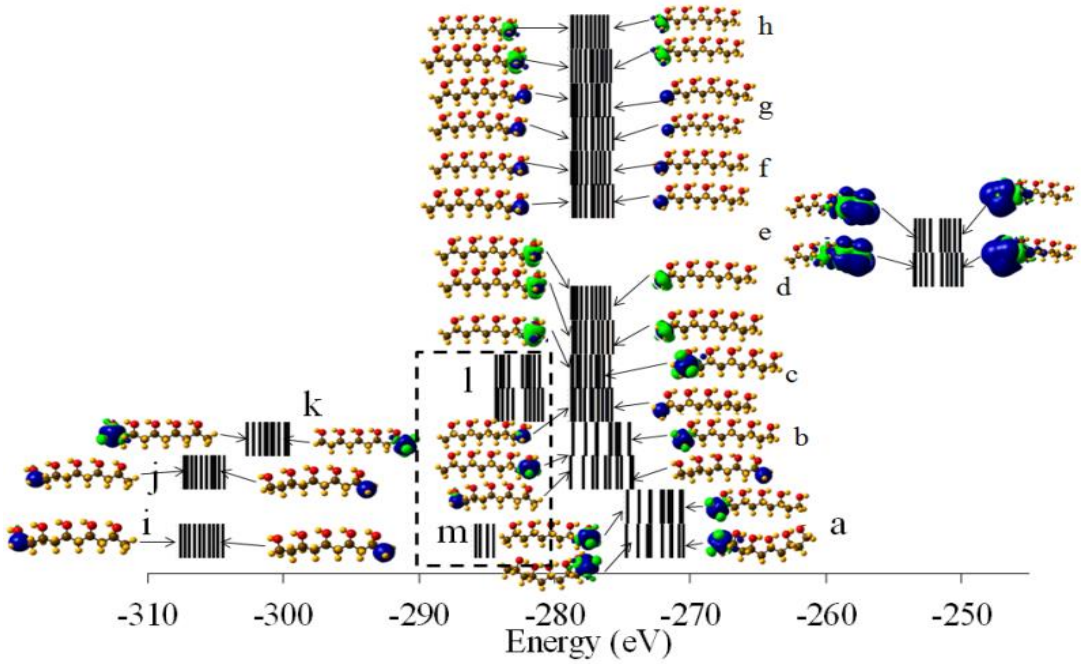

Figure 29. Molecular orbitals of PVA and PVA-5 using B3PW91 with (a) STO-3G, (b) STO-6G, (c) 6-31G*, (d) 7-31G*, (e) 10-31G*, (f) 12-31G*, (g) 16-31G*, (h) cc-pvDZ, MP2 with (i) 6-31G(d), HF with (j) 6-31G(d), (k) STO-3G, (l) 10-31G(d), and (m) experiment.

Figure 30 displays the $C_{10}H_{19}O_5$, $C_{10}H_{20}O_6$, and $C_{10}H_{22}O_5$ (from the bottom to the top) and their corresponding molecular orbital shapes (using HF/10-31G (d)) which are localized depending of the functional group. When the carbonyl group (C=O) and carboxylated group (O-C=O) are added to the PVA the absolute value for the core energy increases in the same trend as it is observed experimentally (Figure 30, bottom lines). The stretching of PVA with O-C=O functional groups does not yield any changes in the core BE as shown in Figure 30 (dashed square). Table 8 shows the total energy and the theoretical value for temperature. There is a correlation factor of ~300 between the change of theoretical and experimental temperature.

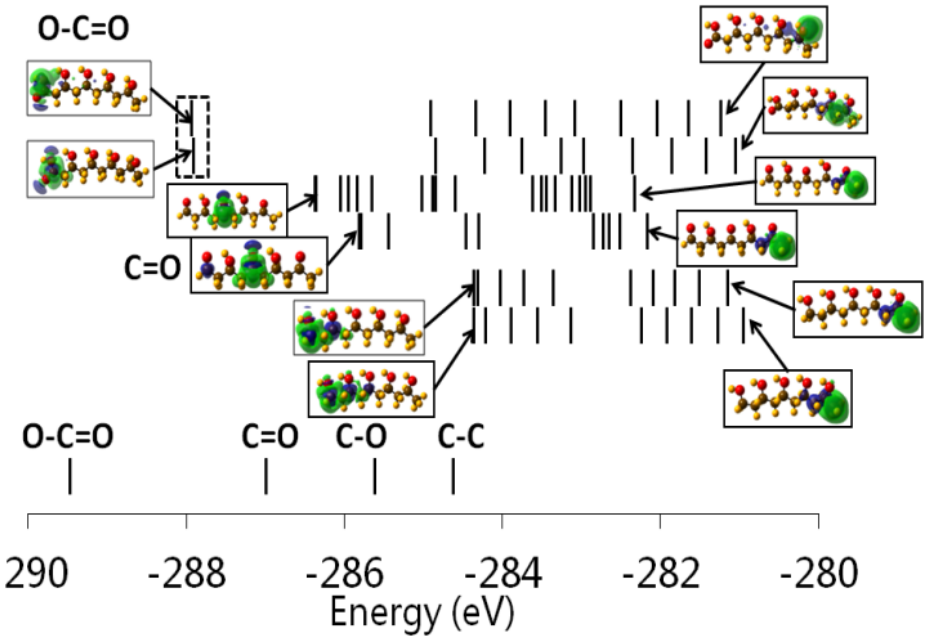

Figure 30. Molecular orbitals energies for PVA and PVA-5 using B3PW91 HF/10-31G (d). Molecular orbital surfaces are plotted with an isovalue of 0.002 and iso-density of 0.0004.

Table 8. Energies of $C_{10}H_{19}O_5$, $C_{10}H_{20}O_6$, and $C_{10}H_{22}O_5$ and when are stretched in 5%. ΔE corresponds to the change of energy (Ha) and ΔT to the change of temperature calculated from the expression $\Delta E \approx K\Delta T$. f is the correlation factor between experiment and theory.

Fig.	Mol. Struc.	E-PVA (Ha)	E-PVA-5% (Ha)
23(a)	$C_{10}H_{20}O_6$	-756.17349	-756.13927
24(b)	$C_{10}H_{19}O_5$	-750.05417	-750.02093
25(c)	$C_{10}H_{20}O_6$	-825.68493	-825.65028

CHAPTER VI

CONCLUSIONS*

Carbon nanotubes have an elastic modulus of 1.3 TPa which was estimated using ab initio calculations. Armchair and chiral nanotubes have ductile deformation fracture while zigzag ones have both ductile, and brittle. Armchair nanotubes break forming two caps while chiral nanotubes adopt a helical-structure conformation at fracture. HOMO-LUMO energy gaps of all the nanotubes decrease at yield strength and then increase after their tensile strength. Thus, deformed CNT (n,n) with n=4,5; CNT (m,0) with m=8 and 10; and CNT (6,2) can be suitable materials for the fabrication of solar cells with electromagnetic absorption in the range of 1.26-2.52 eV. Mechanical properties affect electronic properties of CNTs and can be used to control their electromagnetic absorption properties.

Electron transport in silicon lithium nanoelectrodes decreases as the thickness increases. Higher electrical current is obtained when SEI is composed mainly of Li_2O than LiF. MEP results show that LiF molecules have alternated negative and positive potentials that may hamper the electron mobility.

---

* Part of this chapter is reprinted with permission from:
Coupling of Mechanical and Electronic Properties of Carbon Nanotubes, by D. Cristancho, L. Benitez, and J.M. Seminario, 2013. J. Mol. Model. 19. 5237-5244. Copyright 2013 by Springer-Verlag Berlin Heidelberg.

Degradation of Polyvinyl Alcohol under Mechanothermal Stretching, by D. Cristancho et al., 2013. J. Mol. Model. 19: 3245-3253. Copyright 2013 by Springer-Verlag Berlin Heidelberg.

Electron transport is not affected by the composition and thickness of non-bonded SEI when the electrolyte is present. This is because HOMO-LUMO gap and the transmission function around the Fermi level are not affected as the thickness of SEI is from 20-30 Å. However, when SEI is conformed of bonded Li_2O, electron transport is affected due to Li2O molecules are twisted.

We also investigated the effects of mechano-thermal forces on PVA molecular structure. Standard carbon peaks in PVA were characterized using in situ XPS combined with ab initio calculations. Under mechanical stretching and thermal expansion, the standard peaks of C(1S) shift toward higher binding energies. Core electrons in carbon bonded to oxygen (C-O) are more stable at the range of temperatures 310 K-345 K. This is also corroborated with calculations at the HF/10-31G(d) level of theory. All binding energies for carbon standard peaks were reproduced with an accuracy of 99.2%, setting precise references for future studies regarding the bonding nature and strength of polymers. Finally, the fact that HF yields better results than several of the DFT calculations for the core electrons could be a reason of the major accuracy problems in present functional.

REFERENCES

1. Arico, A. S.; Bruce, P.; Scrosati, B.; Tarascon, J. M.; Van Schalkwijk, W., Nanostructured materials for advanced energy conversion and storage devices. *Nature Materials* **2005,** *4* (5), 366-377.

2. Yakobson, B. I.; Avouris, P., Mechanical properties of carbon nanotubes. *Carbon Nanotubes* **2001,** *80*, 287-327.

3. Rossi, M.; Meo, M., On the estimation of mechanical properties of single-walled carbon nanotubes by using a molecular-mechanics based FE approach. *Composites Science and Technology* **2009,** *69* (9), 1394-1398.

4. Lei, X.; Natsuki, T.; Shi, J.; Ni, Q.-Q., Analysis of carbon nanotubes on the mechanical properties at atomic scale. *J. Nanomaterials* **2011,** *2011*, 1-10.

5. Dresselhaus, M. S.; Dresselhaus, G.; Charlier, J. C.; Hernandez, E., Electronic, thermal and mechanical properties of carbon nanotubes. *Philosophical Transactions of the Royal Society a-Mathematical Physical and Engineering Sciences* **2004,** *362* (1823), 2065-2098.

6. Hassanien, A.; Tokumoto, M.; Kumazawa, Y.; Kataura, H.; Maniwa, Y.; Suzuki, S.; Achiba, Y., Atomic structure and electronic properties of single-wall carbon nanotubes probed by scanning tunneling microscope at room temperature. *Applied Physics Letters* **1998,** *73* (26), 3839-3841.

7. Odom, T. W.; Huang, J. L.; Kim, P.; Lieber, C. M., Atomic structure and electronic properties of single-walled carbon nanotubes. *Nature* **1998,** *391* (6662), 62-64.

8. Ramuz, M. P.; Vosgueritchian, M.; Wei, P.; Wang, C.; Gao, Y.; Wu, Y.; Chen, Y.; Bao, Z., Evaluation of Solution-Processable Carbon-Based Electrodes for All-Carbon Solar Cells. *ACS Nano* **2012,** *6* (11), 10384-10395.

9. Arnold, M. S.; Zimmerman, J. D.; Renshaw, C. K.; Xu, X.; Lunt, R. R.; Austin, C. M.; Forrest, S. R., Broad Spectral Response Using Carbon Nanotube/Organic Semiconductor/C60 Photodetectors. *Nano Letters* **2009,** *9* (9), 3354-3358.

10. Bindl, D. J.; Wu, M.-Y.; Prehn, F. C.; Arnold, M. S., Efficiently Harvesting Excitons from Electronic Type-Controlled Semiconducting Carbon Nanotube Films. *Nano Letters* **2010,** *11* (2), 455-460.

11. Ong, P.-L.; Euler, W. B.; Levitsky, I. A., Hybrid solar cells based on single-walled carbon nanotubes/Si heterojunctions. *Nanotechnology* **2010,** *21* (10).

12. Kar, P.; Wang, K.; Liang, H., Force-dominated non-equilibrium oxidation kinetics of tantalum. *Electrochimica Acta* **2008,** *53* (16), 5084-5091.

13. Wang, K.; Kundu, S.; Lee, H.; Liang, H., Formation of Silver Nanochains through Mechanoactivation. *The Journal of Physical Chemistry C* **2009,** *113* (19), 8112-8117.

14. (a) Wang, K.; Liu, Z.; Cruz, T. H.; Salmeron, M.; Liang, H., In Situ Spectroscopic Observation of Activation and Transformation of Tantalum Suboxides. *The Journal of Physical Chemistry A* **2010,** *114* (7), 2489-2497; (b) Huitink, D.; Gao, F.; Wang, K.; Liang, H., In Situ Monitoring of Tantalum during Electrochemical-Mechanically Induced Oxidation. *Electrochemical and Solid-State Letters* **2010,** *13* (9), F16-F19.

15. Szczech J; S., J., Nanostructured silicon for high capacity lithium battery anodes. *Energy & Enviromental Science* **2010,** *4*, 56-72.

16. Nadimpalli, S. P. V.; Sethuraman, V. A.; Dalavi, S.; Lucht, B.; Chon, M. J.; Shenoy, V. B.; Guduru, P. R., Quantifying capacity loss due to solid-electrolyte-interphase layer formation on silicon negative electrodes in lithium-ion batteries. *Journal of Power Sources* **2012,** *215*, 145-151.

17. Verma, P.; Maire, P.; Novak, P., A review of the features and analyses of the solid electrolyte interphase in Li-ion batteries. *Electrochimica Acta* **2010,** *55* (22), 6332-6341.
18. Cristancho, D.; Seminario, J. M., Polypeptides in alpha-helix conformation perform as diodes. *The Journal of Chemical Physics* **2010,** *132* (6).

19. Hohenberg, P.; Kohn, W., Inhomogeneous Electron Gas. *Physical Review* **1964,** *136* (3B), B864-B871.

20. Kohn, W.; Sham, L. J., Self-Consistent Equations Including Exchange and Correlation Effects. *Physical Review* **1965,** *140* (4A), A1133-A1138.

21. Collins, J. B.; Schleyer, P. V.; Binkley, J. S.; Pople, J. A., Self-Consistent Molecular-Orbital Methods.17. Geometries and Binding Energies of 2nd-row molecules-Comparison of 3 Basis sets. *Journal of Chemical Physics* **1976,** *64* (12), 5142-5151.

22. Becke, A. D., Density Functional Exchange-Energy Approximation with Correct Asymptotic-Behaviour. *Physical Review A* **1988,** *38* (6), 3098-3100.

23. Perdew, J. P.; Wang, Y., Accurate and simple analytic representation of the electron-gas correlation energy. *Physical Review B* **1992,** *45* (23), 13244-13249.

24. Hay, P. J.; Wadt, W. R., Ab initio effective core potentials for molecular calculations. Potentials for the transition metal atoms Sc to Hg. *The Journal of Chemical Physics* **1985,** *82* (1), 270-283.

25. Roy, L. E.; Hay, P. J.; Martin, R. L., Revised Basis Sets for the LANL Effective Core Potentials. *Journal of Chemical Theory and Computation* **2008,** *4* (7), 1029-1031.

26. Murray J; Seminario J; Concha M; P., P., An Analysis of Molecular Electrostatic Potentials Obtained by a Local Density Functional Approach *Intrnational Journal of Quantum Chemistry* **1992,** *44*, 113-122.

27. Frisch, M. J. T., G. W.; Schlegel, H. B.; Scuseria, G. E.;; Robb, M. A. C., J. R.; Scalmani, G.; Barone, V.; Mennucci, B.;; Petersson, G. A. N., H.; Caricato, M.; Li, X.; Hratchian, H. P.;; Izmaylov, A. F. B., J.; Zheng, G.; Sonnenberg, J. L.; Hada, M.;; Ehara, M. T., K.; Fukuda, R.; Hasegawa, J.; Ishida, M.; Nakajima,; T.; Honda, Y. K., O.; Nakai, H.; Vreven, T.; Montgomery, J.; J. A.,; Peralta, J. E. O., F.; Bearpark, M.; Heyd, J. J.; Brothers, E.; Kudin,; K. N.; Staroverov, V. N. K., R.; Normand, J.; Raghavachari, K.;; Rendell, A. B., J. C.; Iyengar, S. S.; Tomasi, J.; Cossi, M.; Rega,; N.; Millam, N. J. K., M.; Knox, J. E.; Cross, J. B.; Bakken, V.;; Adamo, C. J., J.; Gomperts, R.; Stratmann, R. E.; Yazyev, O.;; Austin, A. J. C., R.; Pomelli, C.; Ochterski, J. W.; Martin, R. L.;; Morokuma, K. Z., V. G.; Voth, G. A.; Salvador, P.; Dannenberg, J. J.; Dapprich, S.; Daniels, A. D.; O. Farkas, Foresman, J. B.; €; Ortiz, J. V. C., J.; , Fox, D. J. Gaussian 09, revision A.02; CT,; W *Gaussian, Inc.*, 2009.

28. Roetti., C. *Quantum-Mechanical Ab-Initio Calculation of the Properties of Crystalline Materials.* , Springer-Verlag: 1996.

29. NM., O. B., GaussSum 2.1. *J. Comp. Chem.* **2007,** *29*, 839-845.

30. Dill, J. D.; Pople, J. A., Self-Consistent Molecular-Orbital Method.15. Extended Gaussian-Type Basis Sets for Lithium, Berylium and Boron. *Journal of Chemical Physics* **1975,** *62* (7), 2921-2923.

31. Seeger, R.; Pople, J. A., Self-Consistent Molecular-Orbital Methods.16. Numerically Stable Direct Energy MInimization procedures for solution of Hartree-Fock Equations. *Journal of Chemical Physics* **1976,** *65* (1), 265-271.

32. Petersson, G. A.; Bennett, A.; Tensfeldt, T. G.; Allaham, M. A.; Shirley, W. A.; Mantzaris, J., A complete Basis Set Model Chemistry .1. The Total Energies of Closed-Shell Atoms and Hydrides of the 1st-Row Elements. *Journal of Chemical Physics* **1988,** *89* (4), 2193-2218.

33. Zhu, H. W.; Xu, C. L.; Wu, D. H.; Wei, B. Q.; Vajtai, R.; Ajayan, P. M., Direct synthesis of long single-walled carbon nanotube strands. *Science* **2002,** *296* (5569), 884-886.

34. Kalamkarova, A. L.; Georgiadesa, A. V.; Rokkama, S. K.; Veedub, V. P.; M.N., G.-N., Analytical and numerical techniques to predict carbon nanotubes properties. *International Journal of Solids and Structures* **2006,** *43*, 6832–6834.

35. Minary-Jolandan M.; M., Y., Mechanical and Electromechanical Characterization of One-Dimensional Piezoelectric Nanomaterials. In *Piezoelectric Nanomaterials for Biomedical Applications*, Ciofani G; A., M., Eds. Springer Berlin Heidelberg: 2012; pp 63-91.

36. Wong, E. W.; Sheehan, P. E.; Lieber, C. M., Nanobeam mechanics: Elasticity, strength, and toughness of nanorods and nanotubes. *Science* **1997,** *277* (5334), 1971-1975.

37. Treacy, M. M. J.; Ebbesen, T. W.; Gibson, J. M., Exceptionally high Young's modulus observed for individual carbon nanotubes. *Nature* **1996,** *381* (6584), 678-680.

38. Poncharal, P.; Wang, Z. L.; Ugarte, D.; de Heer, W. A., Electrostatic deflections and electromechanical resonances of carbon nanotubes. *Science* **1999,** *283* (5407), 1513-1516.

39. Campbell, F. C., *Elements of metallurgy and engineering alloys*. ASM International: Materials Park, Ohio, 2008.

40. Krishnan, A.; Dujardin, E.; Ebbesen, T. W.; Yianilos, P. N.; Treacy, M. M. J., Young's modulus of single-walled nanotubes. *Physical Review B* **1998,** *58* (20), 14013-14019.

41. Van Lier, G.; Van Alsenoy C; Van Doren V; Geerlings P, Ab initio study of the elastic properties of single-walled carbon nanotubes and graphene. *Chemical Physics Letters* **2000,** *326* (1-2), 181-185.

42. Natsuki T; Endo M, Structural dependence of nonlinear elastic properties for carbon nanotubes using a continuum analysis. *Applied Physics a-Materials Science & Processing* **2005,** *80* (7), 1463-1468.

43. Pantano, A.; Parks D. M.; Boyce M. C., Mechanics of Deformation and Multi Wall Carbon Nanotubes. *J. Mech. Phys. Solids* **2004,** *52* (4), 789-821.

44. Xuemei, W.; Vijay, G.; Soumendra, N. B., Effects of Substrate Orientation and Metal Film Thickness on the Intrinsic Strength, Intrinsic Fracture Energy, and Total

Fracture Energy of Tantalum–Sapphire Interfaces. *Journal of the American Ceramic Society* **2005,** *88* (7), 1909-1913.

45. Wu Yongdong; Zhang Xiaochun; Leung A. Y. T; Zhong Weifang, An energy-equivalent model on studying the mechanical properties of single-walled carbon nanotubes. *Thin-Walled Structures* **2006,** *44* (6), 667-676.

46. Khoury E; Messager T; P., C., Derivation of the Young's and Shear Moduli of Single-Walled Carbon Nanotubes Through a Computational Homogenization Approach. *Journal for Multiscale Computational Engineering* **2011,** *9*, 97-118.

47. Mylvaganam, K.; Zhang, L. C., Important issues in a molecular dynamics simulation for characterising the mechanical properties of carbon nanotubes. *Carbon* **2004,** *42* (10), 2025-2032.

48. Wu, Y.; Huang, M.; Wang, F.; Huang, X. M. H.; Rosenblatt, S.; Huang, L.; Yan, H.; O'Brien, S. P.; Hone, J.; Heinz, T. F., Determination of the Young's Modulus of Structurally Defined Carbon Nanotubes. *Nano Letters* **2008,** *8* (12), 4158-4161.

49. Shokrieh, M. M.; Rafiee, R., Prediction of Young's modulus of graphene sheets and carbon nanotubes using nanoscale continuum mechanics approach. *Materials & Design* **2010,** *31* (2), 790-795.

50. Arenal, R.; Wang, M.-S.; Xu, Z.; Loiseau, A.; Golberg, D., Young modulus, mechanical and electrical properties of isolated individual and bundled single-walled boron nitride nanotubes. *Nanotechnology* **2011,** *22* (26).

51. Rafiee, R.; Heidarhaei, M., Investigation of chirality and diameter effects on the Young's modulus of carbon nanotubes using non-linear potentials. *Composite Structures* **2012,** *94* (8), 2460-2464.

52. Pop, E.; Mann, D.; Wang, Q.; Goodson, K. E.; Dai, H. J., Thermal conductance of an individual single-wall carbon nanotube above room temperature. *Nano Letters* **2006,** *6* (1), 96-100.

53. Spear; Dismukes, *Synthetic Diamond – Emerging CVD Science and Technology*. 1994.

54. Ci, L.; Suhr, J.; Pushparaj, V.; Zhang, X.; Ajayan, P. M., Continuous carbon nanotube reinforced composites. *Nano Letters* **2008,** *8* (9), 2762-2766.

55. Bakshi, S. R.; Lahiri, D.; Agarwal, A., Carbon nanotube reinforced metal matrix composites - a review. *International Materials Reviews* **2010,** *55* (1), 41-64.

56. Chen, Y. L.; Liu, B.; Huang, Y.; Hwang, K. C., Fracture Toughness of Carbon Nanotube-Reinforced Metal- and Ceramic-Matrix Composites. *J.Nano Mat* **2011**.

57. Ren, J.; Li, L.; Chen, C.; Chen, X.; Cai, Z.; Qiu, L.; Wang, Y.; Zhu, X.; Peng, H., Twisting Carbon Nanotube Fibers for Both Wire-Shaped Micro-Supercapacitor and Micro-Battery. *Advanced Materials* **2013,** *25* (8), 1155-1159.

.

58. Rangel N; Sotelo J. C.; Seminario J. M., Mechanism of Carbon Nanotubes Unzipping into Graphene Ribbons. *J. Chem. Phys* **2009,** *131*.

59. (a) Bobadilla A. D.; Samuel E. L. G.; Tour J. M.; Seminario J. M., Calculating the Hydrodynamic Volume of Poly(ethylene oxylated) Single-Walled Carbon Nanotubes and Hydrophilic Carbon Clusters. *J. Phys. Chem B.* **2013,** *117*, 343-354; (b) Moore, T. L.; Pitzer, J. E.; Podila, R.; Wang, X.; Lewis, R. L.; Grimes, S. W.; Wilson, J. R.; Skjervold, E.; Brown, J. M.; Rao, A.; Alexis, F., Multifunctional Polymer-Coated Carbon Nanotubes for Safe Drug Delivery. *Particle & Particle Systems Characterization* **2013,** *30* (4), 365-373.

60. Wilson, N. R.; Macpherson, J. V., Carbon nanotube tips for atomic force microscopy. *Nat. Nanotechnol.* **2009,** *4* (8), 483-491.

61. Zanello, L. P.; Zhao, B.; Hu, H.; Haddon, R. C., Bone cell proliferation on carbon nanotubes. *Nano Letters* **2006,** *6* (3), 562-567.

62. Aliev, A. E.; Oh, J.; Kozlov, M. E.; Kuznetsov, A. A.; Fang, S.; Fonseca, A. F.; Ovalle, R.; Lima, M. D.; Haque, M. H.; Gartstein, Y. N.; Zhang, M.; Zakhidov, A. A.; Baughman, R. H., Giant-Stroke, Superelastic Carbon Nanotube Aerogel Muscles. *Science* **2009,** *323* (5921), 1575-1578.

63. Liao, Y.; Zhang, C.; Zhang, Y.; Strong, V.; Tang, J.; Li, X.-G.; Kalantar-zadeh, K.; Hoek, E. M. V.; Wang, K. L.; Kaner, R. B., Carbon Nanotube/Polyaniline Composite Nanofibers: Facile Synthesis and Chemosensors. *Nano Letters* **2011,** *11* (3), 954-959.

64. Keefer, E. W.; Botterman, B. R.; Romero, M. I.; Rossi, A. F.; Gross, G. W., Carbon nanotube coating improves neuronal recordings. *Nature Nanotechnology* **2008,** *3* (7), 434-439.

65. Shi, E.; Zhang, L.; Li, Z.; Li, P.; Shang, Y.; Jia, Y.; Wei, J.; Wang, K.; Zhu, H.; Wu, D.; Zhang, S.; Cao, A., TiO2-Coated Carbon Nanotube-Silicon Solar Cells with Efficiency of 15%. *Scientific Reports* **2012,** *2*.

66. Baac, H. W.; Ok, J. G.; Maxwell, A.; Lee, K.-T.; Chen, Y.-C.; Hart, A. J.; Xu, Z.; Yoon, E.; Guo, L. J., Carbon-Nanotube Optoacoustic Lens for Focused Ultrasound Generation and High-Precision Targeted Therapy. *Scientific Reports* **2012,** *2*.

67. Nasibulin, A. G.; Shandakov, S. D.; Nasibulina, L. I.; Cwirzen, A.; Mudimela, P. R.; Habermehl-Cwirzen, K.; Grishin, D. A.; Gavrilov, Y. V.; Malm, J. E. M.; Tapper, U.; Tian, Y.; Penttala, V.; Karppinen, M. J.; Kauppinen, E. I., A novel cement-based hybrid material. *New Journal of Physics* **2009,** *11*.

68. Dalton, A. B.; Collins, S.; Munoz, E.; Razal, J. M.; Ebron, V. H.; Ferraris, J. P.; Coleman, J. N.; Kim, B. G.; Baughman, R. H., Super-tough carbon-nanotube fibres - These extraordinary composite fibres can be woven into electronic textiles. *Nature* **2003,** *423* (6941), 703-703.

69. Zhao, Z.; Gou, J., Improved fire retardancy of thermoset composites modified with carbon nanofibers. *Science and Technology of Advanced Materials* **2009,** *10* (1).

70. Bobadilla A. D.; Samuel E. L. G.; Tour J. M.; M., S. J., Calculating the Hydrodynamic Volume of Poly(ethylene oxylated) Single-Walled Carbon Nanotubes and Hydrophilic Carbon Clusters. *J. Phys. Chem B.* **2013,** *117*, 343-354.

71. Bobadilla, A. D.; Seminario, J. M., DNA-CNT Interactions and Gating Mechanism Using MD and DFT. *Journal of Physical Chemistry C* **2011,** *115* (8), 3466-3474.

72. Seminario, J. M.; Agapito, L. A.; Figueroa, H. P.; Ieee, I., *Towards the design of programmable self-assembled DNA-carbon nanotubes: An approach to nanobiotronics*. 2002.

73. Rangel, N. L.; Sotelo, J. C.; Seminario, J. M., Mechanism of carbon nanotubes unzipping into graphene ribbons. *Journal of Chemical Physics* **2009,** *131* (3).

74. Raghavachari, K., Perspective on "Density functional thermochemistry. III. The role of exact exchange" - Becke AD (1993) J Chem Phys 98:5648-52. *Theoretical Chemistry Accounts* **2000,** *103* (3-4), 361-363.

75. Coluci, V. R.; Pugno, N. M.; Dantas, S. O.; Galvao, D. S.; Jorio, A., Atomistic simulations of the mechanical properties of 'super' carbon nanotubes. *Nanotechnology* **2007,** *18* (33).

76. E., P., The Electrochemical Behaviour of Alkali and Alkaline Earth Metals in Nonaqueos Battery Systems-The Solid Electrolyte Interphase Model. *Electrochemical Society* **1979**.

77. Use and development of PVA Emulsions in field of paper, coating, paint and adhesives. *Journal of the Oil & Colour Chemists Association* **1969,** *52* (10), 981-&.

78. Gao, F.; Liang, H., Transformable Oxidation of Tantalum in Electrochemical Mechanical Polishing (ECMP). *Journal of Electronic Materials* **2011,** *40* (2), 134-140.
79. Huitink, D.; Gao, F.; Liang, H., Tribo-electrochemical surface modification of tantalum using in situ AFM techniques. *Scanning* **2010,** *32* (5), 336-344.

80. Ryu, Y.-G.; Lee, S.; Mah, S.; Lee, D. J.; Kwon, K.; Hwang, S.; Doo, S., Electrochemical behaviors of silicon electrode in lithium salt solution containing alkoxy silane additives. *Journal of the Electrochemical Society* **2008,** *155* (8), A583-A589.

81. Wu, H.; Chan, G.; Choi, J. W.; Ryu, I.; Yao, Y.; McDowell, M. T.; Lee, S. W.; Jackson, A.; Yang, Y.; Hu, L.; Cui, Y., Stable cycling of double-walled silicon nanotube battery anodes through solid-electrolyte interphase control. *Nature Nanotechnology* **2012,** *7* (5), 309-314.

82. Liu, N.; Wu, H.; McDowell, M. T.; Yao, Y.; Wang, C.; Cui, Y., A Yolk-Shell Design for Stabilized and Scalable Li-Ion Battery Alloy Anodes. *Nano Letters* **2012,** *12* (6), 3315-3321.

83. Budi, A.; Basile, A.; Opletal, G.; Hollenkamp, A. F.; Best, A. S.; Rees, R. J.; Bhatt, A. I.; O'Mullane, A. P.; Russo, S. P., Study of the Initial Stage of Solid Electrolyte Interphase Formation upon Chemical Reaction of Lithium Metal and N-Methyl-N-Propyl-Pyrrolidinium-Bis(Fluorosulfonyl)Imide. *The Journal of Physical Chemistry C* **2012,** *116* (37), 19789-19797.

84. Lin, Z. P., Evaluation on two PVA adhesives for gluing transformer insulating components. In *Proceedings: Electrical Electronics Insulation Conference and Electrical Manufacturing & Coil Winding Conference*, Castaldi, T. E., Ed. IEEE Xplore: Rosemont, IL, 1995; pp 119-121.

85. Plyusnina, A. I.; Tolmachev, I. A.; Okhrimenko, I. S., Influences of surfactants (SF) on acid-hydrolisis of polyvinyl acetate(PVA) in aqueos dispersions. *Journal of Applied Chemistry of the Ussr* **1976,** *49* (9), 2103-2105.

86. Mohrova, J.; Kalinova, K., Different Structures of PVA Nanofibrous Membrane for Sound Absorption Application. *Journal of Nanomaterials* **2012**.

87. Hassan, C. M.; Peppas, N. A., Structure and applications of poly(vinyl alcohol) hydrogels produced by conventional crosslinking or by freezing/thawing methods. In *Biopolymers/Pva Hydrogels/Anionic Polymerisation Nanocomposites*, Abe, A., Ed. 2000; Vol. 153, pp 37-65.

88. Kanbara, H.; Huang, S. J.; Johnson, J. F., Measurements of cross-linking degree for electron-beam irradiated block polymers. *Polym Eng Sci* **1994,** *34* (8), 691-694.

89. Tomoda, Y.; Tsuda, M., Importance of Hydroxyl Radicals as Intermediates in Cross-linking of High Polymers by Gamma-Irradiation. *Nature* **1961,** *190* (477), 905-&.
90. Tillet, G.; Boutevin, B.; Ameduri, B., Chemical reactions of polymer crosslinking and post-crosslinking at room and medium temperature. *Progress in Polymer Science* **2011,** *36* (2), 191-217.

91. Akhter, S.; Allan, K.; Buchanan, D.; Cook, J. A.; Campion, A.; White, J. M., XPS and IR Study of X-RAY-Induced degradation of PVA polymer film. *Applied Surface Science* **1988,** *35* (2), 241-258.

92. Beamson, G.; Briggs, D., Degradation of poly(vinyl alcohol) thin films during monochromatized XPS: Substrate effects and x-ray intensity dependence. *Surface and Interface Analysis* **1998,** *26* (5), 343-351.

93. Grass, M. E.; Karlsson, P. G.; Aksoy, F.; Lundqvist, M.; Wannberg, B.; Mun, B. S.; Hussain, Z.; Liu, Z., New ambient pressure photoemission endstation at Advanced Light Source beamline 9.3.2. *Review of Scientific Instruments* **2010,** *81* (5).

94. Perdew, J. P.; Burke, K.; Ernzerhof, M., Generalized gradient approximation made simple. *Physical Review Letters* **1996,** *77* (18), 3865-3868.

95. Perdew, J. P.; Burke, K.; Wang, Y., Generalized gradient approximation for the exchange-correlation hole of a many-electron system (vol 54, pg 16 533, 1996). *Physical Review B* **1998,** *57* (23), 14999-14999.

96.) Frisch, M. J. T., G. W.; Schlegel, H. B.; Scuseria, G. E.;; Robb, M. A. C., J. R.; Scalmani, G.; Barone, V.; Mennucci, B.;; Petersson, G. A. N., H.; Caricato, M.; Li, X.; Hratchian, H. P.;; Izmaylov, A. F. B., J.; Zheng, G.; Sonnenberg, J. L.; Hada, M.;; Ehara, M. T., K.; Fukuda, R.; Hasegawa, J.; Ishida, M.; Nakajima,; T.; Honda, Y. K., O.; Nakai, H.; Vreven, T.; Montgomery, J.; J. A.,; Peralta, J. E. O., F.; Bearpark, M.; Heyd, J. J.; Brothers, E.; Kudin,; K. N.; Staroverov, V. N. K., R.; Normand, J.; Raghavachari, K.;; Rendell, A. B., J. C.; Iyengar, S. S.; Tomasi, J.; Cossi, M.; Rega,; N.; Millam, N. J. K., M.; Knox, J. E.; Cross, J. B.; Bakken, V.;; Adamo, C. J., J.; Gomperts, R.; Stratmann, R. E.; Yazyev, O.;; Austin, A. J. C., R.; Pomelli, C.; Ochterski, J. W.; Martin, R. L.;; Morokuma, K. Z., V. G.; Voth, G. A.; Salvador, P.; Dannenberg, J. J.; Dapprich, S.; Daniels, A. D.; O. Farkas, Foresman, J. B.; €; Ortiz, J. V. C., J.; , Fox, D. J. Gaussian 09, revision A.02; CT,; W *Gaussian, Inc.*, 2009.

97. (a) Petersson, G. A.; Allaham, M. A., A Complete Basis Set Model Chemistry .2. Open-Shell Systems and the Total Energies of the 1st-Row Atoms. *Journal of Chemical Physics* **1991,** *94* (9), 6081-6090; (b) Binkley, J. S.; Pople, J. A.; Hehre, W. J., Self-Consistent Molecular-Orbital Methods. 21. Small Split-Valence Basis-Sets for 1st-Row Elements. *Journal of the American Chemical Society* **1980,** *102* (3), 939-947.

98. (a) Wang, K.; Rangel, N. L.; Kundu, S.; Sotelo, J. C.; Tovar, R. M.; Seminario, J. M.; Liang, H., Switchable Molecular Conductivity. *Journal of the American Chemical Society* **2009,** *131* (30), 10447-10451; (b) Gao, F.; Liang, H., Effects of Potential and Mechanical Stimulation on Oxidation of Tantalum During Electrochemical Mechanical Polishing. *Journal of Electronic Materials* **2012,** *41* (3), 624-631; (c) Kar, P.; Wang, K.; Liang, H., Oxidation of Tantalum with Mechanical Force. *Electrochemical and Solid-State Letters* **2008,** *11* (2), C13-C17.

99. Cristancho, D.; Zhou, Y.; Cooper, R.; Huitink, D.; Aksoy, F.; Liu, Z.; Liang, H.; Seminario, J. M., Degradation of polyvinyl alcohol under mechanothermal stretching. *Journal of Molecular Modeling* **2013,** *19* (8), 3245-3253.

100. (a) Gordon, M. S.; Binkley, J. S.; Pople, J. A.; Pietro, W. J.; Hehre, W. J., Self-Consistent Molecular-Orbital Method 22. Small Split-Valence Basis-Sets for 2nd-Row Elements. *Journal of the American Chemical Society* **1982,** *104* (10), 2797-2803; (b) Pietro, W. J.; Francl, M. M.; Hehre, W. J.; Defrees, D. J.; Pople, J. A.; Binkley, J. S., Self-Consistent Molecular-Orbital Methods. 24. Supplemented small Split-Valence Basis-Sets for 2nd-row Elements. *Journal of the American Chemical Society* **1982,** *104* (19), 5039-5048; (c) Newton, M. D.; Lathan, W. A.; Hehre, W. J.; Pople, J. A., Self-Consistent Molecular Orbital Methods.5. Ab-Initio Calculation Equilibrium Geometries and Quadraticforce Constants. *Journal of Chemical Physics* **1970,** *52* (8), 4064-&.

101. Dunning, T. H., Gaussian-Basis sets for use in correlated Molecular Calculations .1. The atoms Boron thorugh Neon and Hydrogen. *Journal of Chemical Physics* **1989,** *90* (2), 1007-1023.

102. (a) Akhter, S.; Jo, S.; Zhou, X. L.; White, J. In *XPS Identification of Al-PVA Complex*, MRS Proceedings, Cambridge Univ Press: 1989; (b) Samir, F.; Benseddik, E.; Corraze, B.; Bernede, C.; Morsli, M.; Bonnet, A.; Conan, A.; Lefrant, S., XPS and Transport Studies of PVA-PPY and PST-PBTH Composites. *Synthetic Metals* **1995,** *69* (1-3), 341-342; (c) Scholes, P. D.; Coombes, A. G. A.; Illum, L.; Davis, S. S.; Watts, J. F.; Ustariz, C.; Vert, M.; Davies, M. C., Detection and determination of surface levels of poloxamer and PVA surfactant on biodegradable nanospheres using SSIMS and XPS. *Journal of Controlled Release* **1999,** *59* (3), 261-278.

103. (a) Choi, D. S.; Huang, S. L.; Huang, M. S.; Barnard, T. S.; Adams, R. D.; Seminario, J. M.; Tour, J. M., Revised structures of N-substituted dibrominated pyrrole derivatives and their polymeric products. Termaleimide models with low optical band gaps. *Journal of Organic Chemistry* **1998,** *63* (8), 2646-2655; (b) Schreiner, P. R.; Fokin, A. A.; Pascal, R. A.; de Meijere, A., Many density functional theory approaches fail to give reliable large hydrocarbon isomer energy differences. *Organic Letters* **2006,** *8* (17), 3635-3638.